Nature manuscript 2018-03-04040B

Comprehensive measurement of pp-chain solar neutrinos with Borexino

The Borexino collaboration*

Abstract

About 99% of the energy of the Sun is produced through sequences of nuclear reactions, initiated by proton-proton (*pp*) fusion, in which hydrogen is converted into helium. Neutrinos emitted by this nuclear fusion chain represent a unique tool for solar and neutrino physics. Here we report the first complete study of all components of the *pp*-chain as performed by the Borexino collaboration: we measure the interaction rates of *pp*, ^{7}Be, and *pep* neutrinos with the highest precision to date, and of ^{8}B neutrinos with the lowest-threshold. We also set a limit on the *hep* neutrino flux. These measurements provide a direct determination of the *pp*-II/*pp*-I branching ratio and a first indication that the temperature profile in the Sun is more compatible with solar models assuming high surface metallicity. At the same time, we determine the survival probability P_{ee} of solar electron neutrinos at different energies, thus probing simultaneously and with high precision the MSW-LMA flavor conversion paradigm in the vacuum and in the matter dominated regimes.

In 1937, G. Gamow and C. F. von Weizsäcker[1,2] suggested that the Sun is powered by a chain of nuclear reactions initiated by proton-proton fusion and leading to the production of ^{4}He. This idea was further developed by H.Bethe and C.Critchfield[3]. In the same years, C. F. von Weizsäcker and independently Bethe proposed an alternative mechanism, namely, the carbon-nitrogen-oxygen cycle (CNO cycle)[4], a closed-loop chain of nuclear reactions catalyzed by ^{12}C, ^{14}N, and ^{16}O nuclei in which four protons are converted into ^{4}He. Although Bethe incorrectly considered the CNO cycle as the main source of energy in the Sun (mainly because of the overestimation of the Sun's central temperature available at that time), the debate on the role of the CNO cycle in the Sun is still relevant today. Indeed, a direct measure of its importance is missing, although theory predicts that it cannot contribute more than about 1% of the solar luminosity. Conversely, it is now understood to be the main source of energy in stars heavier than the Sun. More historical details can be found in[5].

The Sun and lower mass stars are predominantly powered by the proton-proton (*pp*) chain (see Fig. 1), which was thoroughly studied by W. Fowler and co-workers in the 1950s[6]. He and A. Cameron also pointed out that the detection of solar neutrinos (νs) could be a direct way of testing theoretical solar models. The following decades proved them right by elevating neutrinos to be the sole direct probes of the Sun's core and of solar energy generation.

Neutrinos are copiously emitted in the primary proton-proton fusion reaction of the chain (*pp*

* Lists of participants and their affiliations appear at the end of the paper.

νs), and, to a minor extent, in the alternative three-body proton-electron-proton process (*pep* νs) and in the two secondary branches *pp*-II (^{7}Be νs) and *pp*-III (^{8}B νs). Experimentally, solar neutrinos have been studied since the late 1960s by radiochemical experiments (Homestake[7], SAGE[8], and GALLEX[9]) which however could only provide a measurement of the integral rate above a threshold. Prior to Borexino, only ^{8}B neutrinos (<0.01% of the total flux) have been measured individually by KamiokaNDE/ SuperKamiokande[10] and SNO[11]. Their measurements have definitively proven that neutrinos undergo flavor conversion in the Sun's matter, enhanced through the MSW mechanism[13,14]. For an historical review of solar neutrino astronomy and of its impact on solar and neutrino physics see, *e.g.*, [15,16,17].

The measurement of all neutrino components is the most direct way to test the standard solar model (SSM)[15] and to validate our theoretical understanding of the properties of the Sun's core. The first theoretical predictions of neutrino fluxes was put forth in the sixties by J. Bahcall and collaborators, and was subsequently refined to this day by many theoretical groups[18]. Despite the results delivered by solar neutrino experiments, important questions about the Sun remain unanswered. For example, the *solar metallicity*, *i.e.*, the abundance of elements heavier than He, is poorly understood, even though it is a fundamental parameter for the determination of the physical properties of the Sun. A precise measurement of the solar neutrino fluxes comprising the *pp* chain and the CNO cycle would directly settle the open controversy between high (HZ) and low (LZ) metallicity SSMs[18] (see Methods). This paper is a first significant step in this direction.

Solar νs are also powerful probes of neutrino properties. Firstly, they allow the determination of oscillation parameters, especially the θ_{12} mixing angle and, to a lesser degree, the Δm^2_{12} mass splitting. Secondly, the measurement of the electron neutrino survival probability (P_{ee}) as a function of neutrino energy allows one to directly probe the MSW-LMA mechanism of neutrino oscillations[19] and to search for deviations that could indicate the presence of Beyond the Standard Model physics.

Running continuously since 2007, Borexino has measured, one-by-one, ^{7}Be[20,21,22], *pep*[23], ^{8}B[24], and *pp* neutrinos[25]. This paper reports the first simultaneous precision spectroscopic measurement of the complete *pp*-chain and its implications for both solar and neutrino physics.

Borexino and the solar neutrino analysis

Borexino is a liquid scintillator (LS) experiment at the Laboratori Nazionali del Gran Sasso in Italy[26]. Given the tiny cross section of neutrino interactions with electrons ($\sigma \sim 10^{-44} - 10^{-45}$ cm^2 for the solar neutrino energy range), the rates expected in Borexino are small, ranging from less than 1 to few tens of counts per day (cpd) per 100 tons for different solar neutrino components. To cope with such a low event rate, Borexino has a large target mass (~ 300 t) and is housed deep underground, under 3800 meters water equivalent of dolomitic rock that suppress the flux of cosmic radiation approximately one million-fold. For more details on the detector, see Methods.

Radioactive decays of unstable isotopes contained in the scintillator or in the materials surrounding it represent the main source of background (referred to as internal and external, respectively). While external background is greatly reduced by concentric layers of high purity materials surrounding the scintillator and by the selection of a centrally-located software-defined fiducial volume, most of the internal background can only be cut down by means of LS purification. Particularly, β and γ+β interactions must be reduced to very low levels, since they cannot be distinguished from neutrino interactions on an event-by-event basis. Borexino has reached unprecedented levels of scintillator radio-purity. As an example, concentrations of ^{238}U and ^{232}Th are < 9.4 x 10^{-20} g/g and < 5.7 x 10^{-19} g/g (95% C.L.), respectively, ~10 order of magnitude less abundant than in any natural material on Earth. This low level of background has enabled the first real-time detection of solar neutrinos with an energy threshold of 0.19 MeV, and allowed to perform the complete spectroscopy of the *pp*-chain described in this paper.

Solar νs reach the Earth as a mixture of all neutrino flavors (electron, muon, and tau) due to the flavor conversion mechanism enhanced by the MSW effect (see Methods). Borexino detects them by means of their weak elastic scattering off electrons. A fraction of the incoming neutrino energy E_ν is transferred to one electron, which deposits it in the LS. The scintillator light is detected by ~2000 photomultiplier tubes (PMTs), which ensure high detection efficiency of photoelectrons (*p.e.*) produced by incident optical photons at their photocathodes. For ^{7}Be (E_ν = 0.384 and 0.862 MeV) and *pep* (E_ν = 1.44 MeV) neutrinos, the induced electron recoil endpoints are 0.230 MeV, 0.665 MeV, and 1.22 MeV, respectively. For the continuous *pp* and ^{8}B spectra, they are 0.261 MeV and 15.2 MeV, respectively.

The detected light and its time distribution among PMTs yield three important quantities for each interaction event in the detector: its deposited energy, roughly proportional to the total number of detected *p.e.*; its position within the detector, obtained from the analysis of the photon arrival times at each PMT; and its particle identification, based on a *pulse-shape* discrimination method which exploits the different time structure of LS light pulses produced by different particles (electrons, positrons, α, protons..)[27]. For reference, a 1 MeV electron produces on average ~500 *p.e.* in 2000 PMTs, its energy is measured with σ~50 keV, and its position is reconstructed with σ~12 cm.

In this work we have divided the analysis into two energy regions that are affected by different backgrounds, which have to be handled differently: a Low Energy Region (*LER*), (0.19 - 2.93) MeV, to measure the *pp*, ^{7}Be, and *pep* ν interaction rates, and a High Energy Region (*HER*), (3.2 – 16) MeV, to measure ^{8}B-νs. For the same reason, the *HER* is further divided into two sub-regions, below and above 5.7 MeV (*HER-I* and *HER-II*). The measurement of ^{8}B νs cannot be extended below 3.2 MeV because of the 2.614 MeV γ-ray background from ^{208}Tl decays, originating from trace ^{232}Th contamination of the thin nylon LS-containment vessel.

The reconstructed position of each event within the detector allows to define a fiducial volume (FV) optimized differently for the analysis in the *LER* and *HER-I/II*. The *LER* FV is chosen to suppress external γ-rays from ^{40}K, ^{214}Bi, and ^{208}Tl contained in materials surrounding the scintillator and consists of the innermost 71.3 t of scintillator selected with a radial cut ($R<2.8$ m) and a cut in the vertical direction ($1.8<z<2.2$ m). The *HER* is above the energy of the aforementioned γ-rays. The analysis in *HER-I* requires only a $z<2.5$ m cut to suppress background events related to a small pin hole in the inner vessel (IV) that causes LS to leak into the region outside the IV. The total selected mass in this case is 227.8 t. On the contrary, the analysis in *HER-II* uses the entire scintillator volume, 266 t, since the above mentioned background doesn't affect this energy window.

The *LER* analysis uses exclusively Borexino Phase-II data collected between December 2011 and May 2016, in which the internal ^{85}Kr and ^{210}Bi contamination was reduced with respect to Borexino Phase-I, thanks to a LS purification campaign carried on in 2010 and 2011. The total *LER* exposure is 1291.51 days × 71.3 t. With the exception of ^{208}Tl decays (Q ~5 MeV), the *HER* is above natural, long-lived radioactive background, making it possible to use a larger data set, collected between January 2008 and December 2016, for a total exposure of 2062.4 days × 227.8 (266.0) t for *HER-I(II)*, respectively.

The analysis proceeds in two steps: *i)* the event selection, with a different set of cuts in the three energy regions to maximize the signal-to-background ratio, and *ii)* the extraction of the neutrino and residual background rates with a combined fit of distributions of global quantities built for the events surviving the cuts.

The main event selection criteria are conceptually similar for the *LER* and the *HER* and are conceived to: *i)* reject cosmic muons surviving the mountain shield; *ii)* reduce cosmogenic background, *i.e.* radioactive elements produced in muon-induced nuclear spallation processes, and *iii)* select an optimal spatial region of the scintillator (FV). More details on the cuts are discussed in Methods.

Several backgrounds, listed in Table I and described in details in Methods, survive the event selection cuts. In order to disentangle the neutrino signal from these backgrounds, two different fitting strategies are adopted for the low and high energy regions. The *LER* analysis follows a multivariate approach, simultaneously fitting the energy spectrum, the spatial, and the pulse-shape estimator distributions. In the *HER-I/II*, a fit of the radial distribution of events is performed to separate the ^{8}B ν signal (uniformly distributed in the scintillator) from the external background.

Some residual background rates are measured independently, whenever possible, and are constrained in the fit (values between squared brackets in Table I). The remaining background rates are left free to vary and are returned by the fit together with the neutrino rates.

The results of the fit are exemplified in Fig. 2: panel a) shows the energy spectrum in the *LER* after applying the *Three-Fold coincidence* method (TFC) to reduce the ^{11}C cosmogenic background (see Methods); panel b) shows the radial distribution of the events in the *HER-I*. The different contributions from signal and background as determined by the fit are superimposed to data in the plots. The results of the fit for the untagged backgrounds are summarized in Table I.

Results

The high precision solar neutrino results obtained in this work are summarized in Table 2**.** The first column reports the measured rates. In the second column, we translate these measurements into the corresponding solar neutrino fluxes using the known electron and μ/τ neutrino cross sections[27] and the flavor composition calculated according to the MSW-LMA paradigm (mass and mixing parameters from[19]). The third column shows the theoretical fluxes predicted by the Standard Solar Model under the high and low metallicity assumptions[18].

In the *LER* multivariate fit, performed to extract the *pp*, *pep*, and ^{7}Be ν rates, we first constrain the CNO ν interaction rate to the value predicted by the HZ-SSM assuming the MSW-LMA scenario (4.92±0.55 cpd/100t)[18,19], then, separately, to the LZ-SSM predictions (3.52±0.37 cpd/100t). Only the *pep* ν rate is slightly influenced by this constraint and thus two results for it are reported. In both cases, the absence of the *pep* reaction in the Sun is rejected with > 5 σ significance, enough to definitively claim discovery of solar *pep* neutrinos. The contribution of ^{8}B νs in *LER* is very small and its rate was constrained to the value obtained from the *HER* analysis. Statistical uncertainties are evaluated by profiling the likelihood using Wilks's approximation, whose adequacy in this case is confirmed by Monte Carlo (MC) simulations. The ^{7}Be solar ν flux is determined with a total uncertainty of 2.7%, a factor of 1.8 improvement with respect to our previous result[22] and a factor of two smaller than the theoretical uncertainty. The *pp* interaction rate is consistent with our previous result[25] and has an uncertainty of 9.5%. Fits were performed with several hundred configurations, yielding results whose spread is incorporated in the systematic uncertainties (see Methods for more details).

The ^{8}B solar neutrino flux derived from our measured rate in the entire *HER* is $\left(5.68^{+0.39+0.03}_{-0.41-0.03}\right) \times 10^{6}$ cm^{-2} s^{-1}, consistent with our previous result[24] and with the high-precision determination by SuperKamiokande[31] and SNO[32]. The equivalent flavor stable ^{8}B flux, *i.e.,* the flux obtained attributing the measured rate entirely to electron neutrinos, is $\left(2.57^{+0.17+0.07}_{-0.18-0.07}\right) \times 10^{6}$ cm^{-2} s^{-1}. The uncertainty in the ^{8}B rate determination is 8%, a more than 2-fold improvement from our previous measurement[24].

The similarity between the electron recoil spectrum induced by CNO νs and the ^{210}Bi β decay spectrum makes it impossible to disentangle the two contributions with the spectral fit. For this reason, we only provide an upper limit on the CNO neutrino interaction rate. In order to do so, we also place an indirect constraint on *pep* νs by exploiting the theoretically well-known *pp* and *pep* flux ratio. Using values predicted by the HZ-SSM[18] and including the effect of MSW-LMA oscillations[19], the ratio of *pp* and *pep* neutrino interaction rates is $R(pp/pep) = (47.8 \pm 0.8)$. Using the ratio predicted by the LZ-SSM, $R(pp/pep) = (47.5 \pm 0.8)$, yields identical results. We obtain an upper limit of <8.1 cpd/100t (95% C.L.) for the CNO ν interaction rate, in agreement with the Borexino sensitivity to CNO studied with toy MC.

For completeness, we also perform a search for the *hep* neutrinos, emitted by the proton capture reaction on ^{3}He (Fig. 1). The expected flux is more than two orders of magnitude smaller than that of ^{8}B neutrinos. Despite their higher end-point energy, this signal in Borexino is extremely small and covered by background, particularly cosmogenic ^{11}Be decays (Q = 11.5 MeV, β^{-}, τ = 19.9 s) and ^{8}B neutrinos. We perform a dedicated analysis on the whole data set (0.8 kton × y) and in the energy region between (11 -20) MeV; we find 10 ± 3 events, consistent with the expected background. We obtain an upper limit for the *hep* neutrino flux of 2.2×10^{5} cm^{-2} s^{-1} (90% C.L.) to be compared with the expected flux 7.98×10^{3} cm^{-2} s^{-1} (8.25×10^{3} cm^{-2} s^{-1}) assuming HZ (LZ) Solar Standard Model.

Discussion and outlook

The measurements reported in this work represent the first complete study of the solar *pp*-chain and of its different terminations by means of neutrino detection in a single detector and with a uniform data analysis procedure. These measurements can be used either to test the MSW-LMA paradigm assuming SSM flux predictions or, alternatively, to probe our understanding of solar physics assuming the validity of the neutrino oscillation mechanism.

The interaction rates of *pp*, ^{7}Be, *pep*, and ^{8}B neutrinos reported in Table 2 can be used to infer the electron neutrino survival probability at different energies. Assuming the HZ-SSM fluxes[18] and standard neutrino-electron cross sections[27], we obtain the electron neutrino survival probabilities for each solar neutrino component: P_{ee}(*pp,* 0.267 MeV) = 0.57 ± 0.09, P_{ee}(^{7}Be, 0.862 MeV) = 0.53 ± 0.05, and P_{ee}(*pep,* 1.44 MeV) = 0.43 ± 0.11. The quoted errors include the uncertainties on the SSM solar neutrino flux predictions. The ^{8}B electron neutrino survival probability is calculated in each *HER* range following the procedure described in[24]. We obtain P_{ee}($^{8}B_{HER,}$8.1 MeV) = 0.37 ± 0.08, P_{ee}($^{8}B_{HER\text{-}I,}$ 7.4 MeV) = 0.39 ± 0.09, and P_{ee}($^{8}B_{HER\text{-}II,}$ 9.7 MeV) = 0.35 ± 0.09. These results are summarized in Fig. 3. For non mono-energetic components, *i.e.* *pp* and ^{8}B νs, the P_{ee} value is quoted for the average energy of neutrinos which produce scattered electrons in the given energy range.

Borexino provides the most precise measurement of the P_{ee} in the low-energy region, where flavor conversion is vacuum-dominated. At higher energy, where flavor conversion is dominated by matter effects in the Sun, the Borexino results are in agreement with the high-precision measurements performed by SuperKamiokande[31] and SNO[32]. Borexino is the only experiment that can simultaneously test neutrino flavor conversion both in the vacuum and in the matter dominated regime. We performed a likelihood ratio test to compare our data with the MSW-LMA and the vacuum-LMA predictions (pink and grey bands in Fig. 3, respectively). Our data disfavor the vacuum-LMA hypothesis at 98.2% C.L. (see Methods).

Overall, the results are in excellent agreement with the expectations from the MSW-LMA paradigm with the oscillation parameters indicated in[19].

Since solar neutrinos are detected on Earth only about 8 minutes after being produced, they provide a real-time picture of the core of the Sun. In particular, the neutrino fluxes determined experimentally can be used to derive the total power generated by nuclear reactions in the Sun's core[35]. By using exclusively the new Borexino results reported in Table 2, we find $L_{\nu} = (3.89^{+0.35}_{-0.42}) \times 10^{33}$ erg/s, in agreement with the luminosity calculated using the well-measured photon output, L_γ= (3.846 ± 0.015) x 10^{33} erg/s[33,34]. This confirms experimentally the nuclear origin of the solar power with the best precision obtained by a single solar neutrino experiment.

Considering that it takes ~ 10^5 years for radiation to flow from the energy producing region to the surface of the Sun, this comparison proves also that the Sun has been in thermodynamic equilibrium over this timescale.

Furthermore, we derive for the first time the ratio R between the ^{3}He-^{4}He and the ^{3}He-^{3}He fusion rates, which quantifies the relative intensity of the two primary terminations of the *pp* chain (*pp*-II and *pp*-I, see Fig. 1), a critical probe of solar fusion. Neglecting the ^{8}B ν contribution, this ratio can be extracted from the measured *pp* and ^{7}Be ν fluxes by the relation, $R=2\Phi(^7\text{Be})/[\Phi(pp)- \Phi(^7\text{Be})]$ [36]. We find $R = 0.178^{+0.27}_{-0.23}$, in agreement with the most up-to-date predicted values of R = 0.180 ± 0.011 (HZ) and 0.161 ± 0.010 (LZ) [18].

Finally, the Borexino measurements can be used to test the predictions of SSMs with different metallicity. Indeed, the assumed metallicity determines the opacity of solar plasma and, as a consequence, regulates the central temperature of the Sun and the branching ratios of the different pp-chain terminations. In order to perform this test, we use only the results for ^{7}Be and ^{8}B neutrinos, whose fluxes display a significant difference between HZ and LZ-SSM theoretical predictions (9% and 18%, respectively). Figure 4 shows the results of Borexino (green shaded ellipse), together with the predictions for the HZ and LZ-SSMs[18] (blue and red shaded ellipses, respectively). Note that the errors in the Borexino measurements are in both cases smaller than the theoretical uncertainties. The theoretical error budget is dominated by uncertainties on the astrophysical factor S_{34} of the ^{3}He+^{4}He reaction, on the opacity of the Sun, and on the astrophysical factor S_{17} of the p+^{7}Be reaction as discussed in[18].

The Borexino results are compatible with the temperature profiles predicted by both HZ and LZ-SSMs. However, the ^{7}Be and ^{8}B solar neutrino fluxes measured by Borexino provide an interesting hint in favor of the HZ-SSM prediction. A frequentist hypothesis test based on a likelihood-ratio test statistics (HZ vs LZ) was performed by computing the probability distribution functions with a toy Monte Carlo approach. Assuming HZ to be true, our data disfavor LZ at 96.6% C.L. This constraint is slightly stronger than our sensitivity (the median sensitivity is at 94.2% C.L.). A Bayesan hypothesis test[37] yields a Bayes factor of 4.9, confirming a mild preference for HZ (see Methods for more details on both the frequentist and Bayesian studies).

For the sake of completeness, we have performed a global fit including the results presented in this work together with all the other solar + KamLAND data. Following the procedure described in[27], we leave the oscillation parameters θ_{12}, Δm^2_{12}, and the ^{7}Be and ^{8}B neutrino fluxes free to vary in the fit. Figure 4 shows the allowed regions in the $\Phi(^7\text{Be})$-$\Phi(^8\text{B})$ space determined from this global analysis. The oscillation parameters returned by the fit are consistent with the one obtained in[19]. It is clear from the output of this global fit that when the Borexino results are combined with those of all other solar neutrino experiments, the small hint towards HZ further weakens.

In summary, in this work we have reported the first simultaneous measurement of solar neutrinos from all the reactions belonging to the proton-proton nuclear fusion chain. This study confirms the nuclear origin of the solar power and provides the most complete real-time insight into the core of our Sun to date.

Online Content Methods, along with any additional Extended Data display items and Source Data, are available in the online version of the paper; references unique to these sections appear only in the online paper.

References

1. Atkinson, R. & Houtermans, F., Zur Frage der Aufbaumöglichkeit der Elemente in Sternen. *Z. Physik* **54**, 656 (1929).
2. von Weizsacker, C.F., Physikalische Zeitschrift 38 1937 P.176; ibid 39 1938 P.633.
3. Bethe, H. A. and Critchfield, C. L., The formation of deuterons by proton combination. *Phys. Rev.* **54**, 248 (1938).
4. Bethe, H., Energy Production in Stars, *Phys. Rev.* **55**, 434 (1939).
5. Bahcall, J.N., How the Sun Shines. https://www.nobelprize.org/nobel_prizes/themes/physics/fusion/ (2000).
6. Fowler, W., Experimental and Theoretical Nuclear Astrophysics; The Quest for the Origin of the Elements. *Nobel Prize Lecture* (1983).
7. Davis, R., A Half-Century with Solar Neutrinos. *Nobel Prize Lecture* (2002).
8. Abdurashitov, J. *et al*., SAGE coll., Results from SAGE (The Russian-American gallium solar neutrino experiment). *Phys. Lett.* B **328**, 234 (1994).
9. Anselmann, P. *et al*., GALLEX coll., Solar neutrinos observed by GALLEX at Gran Sasso. *Phys. Lett.* B **285**, 376 (1992).
10. Hirata, K. *et al.*, Kamiokande-II coll., Observation of ^{8}B solar neutrinos in the Kamiokande-II detector. *Phys. Rev. Lett.* **63**, 16 (1989).
11. Ahmad, Q. *et al*., SNO coll., Direct Evidence for Neutrino Flavor Transformation from Neutral-Current Interactions in the Sudbury Neutrino Observatory. *Phys. Rev. Lett.* **89,** 011301 (2002).
12. Pontecorvo, B., Neutrino Experiments and the Problem of Conservation of Leptonic Charge. *Zh. Eksp. Teor. Fiz.* **53**, 1717 (1967).
13. Wolfenstein, L., Neutrino oscillations in matter. *Phys. Rev. D* **17**, 2369 (1978).

14. Mikheyev, S. & Smirnov, A., Resonant amplification of neutrino oscillations in matter and spectroscopy of solar neutrinos. *Sov. J. Nucl. Phys.* **42**, 913 (1985).

15. Bahcall, J. and Davis, R., The evolution of neutrino astronomy. *Publ.Astron.Soc.Pac.* **112**, 429 (2000).

16. Haxton, W., Hamish Robertson, R. & Serenelli, A., Solar Neutrinos: Status and Prospects. *Ann. Rev. Astron. Astrophys,* **51**, 21 (2013).

17. Bahcall, John N., *Neutrino Astrophysics*. Cambridge University Press (1989).

18. Vinyoles, N. *et al*., A new Generation of Standard Solar Models. *The Astrophysical Journal* **835**, 202 (2017).

19. Esteban, I. *et al*., Updated fit to three neutrino mixing: exploring the accelerator-reactor complementarity. *Journal of High Energy* Physics **1701,** 087 (2017).

20. Arpesella, C. *et al*., Borexino coll., First real time detection of ^{7}Be solar neutrinos by Borexino. *Phys. Lett*. B **658,** 101 (2008).

21. Arpesella, C. *et al*., Borexino coll., Direct Measurement of the ^{7}Be Solar Neutrino Flux with 192 Days of Borexino Data. *Phys. Rev. Lett.* **101**, 091302 (2008).

22. Bellini, G. *et al*., Borexino coll., Precision measurement of the ^{7}Be solar neutrino interaction rate in Borexino. *Phys. Rev. Lett.* **107**, 141302 (2011).

23. Bellini, G. *et al*., Borexino coll., First evidence of pep solar neutrinos by direct detection in Borexino. *Phys. Rev. Lett.* **108**, 051302 (2012).

24. Bellini, G. *et al*., Borexino coll., Measurement of the solar ^{8}B neutrino rate with a liquid scintillator target and 3 MeV energy threshold in the Borexino detector. *Phys. Rev.* D **82**, 033006 (2010).

25. Bellini, G. *et al*., Borexino coll. Neutrinos from the primary proton-proton fusion process in the Sun. *Nature* **512,** 383 (2014).

26. Alimonti, G. *et al*., Borexino coll., The Borexino detector at the Laboratori Nazionali del Gran Sasso. *Nucl. Instr. and Methods* A **600**, 568 (2009).

27. Bellini, G. *et al*., Borexino coll., Final results of Borexino Phase-I on low-energy solar neutrino spectroscopy. *Phys. Rev*. D **89,** 112007 (2014).

28. Back, H. *et al*., Borexino coll., Borexino calibrations: Hardware, Methods and Results. *JINST* **7**, P10018 (2012).

29. Agostini, M. *et al*., Borexino coll., The Monte Carlo simulation of the Borexino detector. *Astropart. Phys*. **97,** 136 (2018).

30. Bellini, G. *et al*., Borexino coll., Muon and cosmogenic neutron detection in Borexino. *JINST* **6**, P05005 (2012).

31. Abe, K. *et al*., Super-Kamiokande coll., Solar neutrino measurements in Super-Kamiokande-IV. *Phys. Rev.* D **94**, 052010 (2016).

32. Aharmim, B. *et al.*, SNO coll., Combined analysis of all three phases of solar neutrino data from the Sudbury Neutrino Observatory. *Phys. Rev.* C**88**, 025501 (2013).

33. Chapman, G. A., Solar luminosity. *Encyclopedia of Planetary Science. Encyclopedia of Earth Science.* (Springer Netherlands) pp. 748 (1997).

34. Frohlich, C. and Lean, J., The Sun's total Irradiance: Cycles, trends and related climate change uncertainties since 1976. *Geophys. Res. Lett.* **25** issue 23, 4377 (1998).

35. Bergstrom, J. *et al.*, Updated determination of the Solar Neutrino Fluxes from Solar Neutrino Data. *Journal of High Energy Physics* **03,** 132 (2016).

36. Bahcall, J. & Pena-Garay, C., A road map to solar neutrino fluxes, neutrino oscillation parameters and tests for new physics. *Journal of High Energy Physics* **11,** 4 (2003).

37. Caldwell, A., Kollar, D., Kroninger, K., BAT- the Bayesian Analysis Toolkit. *Comput. Phys. Commun.* **180**, 2197 (2009); arXiV:0808.2552.

38. Bahcall, J.N., http://www.sns.ias.edu/~jnb/ (2005).

39. Feng Pen An *et al*., Daya Bay Collaboration, Measurement of electron antineutrinon oscillation based on 1230 days of operation of the Daya Bay experiment. *Phys. Rev.* D **95**, 072006 (2017).

40. Gando, A. et al., KamLAND Collaboration, Reactor On-Off Antineutrino Measurement with KamLAND, *Phys. Rev.* D **88**, 033001 (2013).

Acknowledgements

The Borexino program is made possible by funding from INFN (Italy), NSF (USA), BMBF, DFG, HGF, and MPG (Germany), RFBR (Grants 16-29-13014 ofi-m, 17-02-00305 A), RSF (Grant 17-12-01009) (Russia), and NCN (Grant No. UMO 2017/26/M/ST2/00915) (Poland). We acknowledge also the computing services of Bologna INFN-CNAF data centre and LNGS Computing and Network Service (Italy), of Jülich Supercomputing Centre at FZJ (Germany), and of ACK Cyfronet AGH Cracow (Poland). We acknowledge the generous hospitality and support of the Laboratori Nazionali del Gran Sasso (Italy).

Author Contributions:

The Borexino detector was designed, constructed, and commissioned by the Borexino Collaboration over the span of more than 15 years. The Borexino Collaboration sets the science goals. Scintillator purification and handling, source calibration campaigns, PMT and electronics operations, signal processing and data acquisition, MC simulations of the detector, and data analyses were performed by Borexino members who also discussed and approved the scientific results. This manuscript was prepared by a subgroup of authors appointed by the Collaboration and subjected to an internal collaboration-wide review process. All authors reviewed and approved the final version of the manuscript.

Author Information:

Reprints and permissions information is available at www.nature.com/reprints. The authors declare no competing financial interests. Readers are welcome to comment on the online version of this article at www.nature.com/nature. Correspondence and requests for materials should be addressed to spokesperson-borex@lngs.infn.it .

* **Borexino Collaboration:**

M. Agostini[17], K. Altenmüller[17], S. Appel[17], V. Atroshchenko[7], Z. Bagdasarian[25], D. Basilico[10], G. Bellini[10], J. Benziger[14], D. Bick[4], G. Bonfini[9], D. Bravo[10,f], B. Caccianiga[10], F. Calaprice[13], A. Caminata[3], S. Caprioli[10], M. Carlini[9], P. Cavalcante [9,16], A. Chepurnov[18], K. Choi[24], L. Collica[10], D. D'Angelo[10], S. Davini[3], A. Derbin[12], X.F. Ding[9,19], A. Di Ludovico[13], L. Di Noto[3], I. Drachnev[12], K. Fomenko[2], A. Formozov[2,10,18], D. Franco[1], F. Gabriele[9], C. Galbiati[13], C. Ghiano[9], M. Giammarchi[10], A. Goretti[9], M. Gromov[18], D. Guffanti[9,19], C. Hagner[4], T. Houdy[1], E. Hungerford[20], Aldo Ianni[9,a], Andrea Ianni[13], A. Jany[5], D. Jeschke[17], V. Kobychev[6], D. Korablev[2], G. Korga[20], D. Kryn[1], M. Laubenstein[9], E. Litvinovich[7,8], F. Lombardi[9,b], P. Lombardi[10], L. Ludhova[25,26], G. Lukyanchenko[7], L. Lukyanchenko[7], I. Machulin[7,8], G. Manuzio[3], S. Marcocci[9,19,e], J. Martyn[23], E. Meroni[10], M. Meyer[21], L. Miramonti[10], M. Misiaszek[5], V. Muratova[12], B. Neumair[17], L. Oberauer[17], B. Opitz[4], V. Orekhov[7], F. Ortica[11], M. Pallavicini[3], L. Papp[17], Ö. Penek[25,26], N. Pilipenko[12], A. Pocar[15], A. Porcelli[23], G. Raikov[7], G. Ranucci[10], A. Razeto[9], A. Re[10], M. Redchuk[25,26], A. Romani[11], R. Roncin[1,9], N. Rossi[9,c], S. Schönert[17], D. Semenov[12], M. Skorokhvatov[7,8], O. Smirnov[2], A. Sotnikov[2], L.F.F. Stokes [9], Y. Suvorov[7,22,d], R. Tartaglia[9], G. Testera[3], J. Thurn[21], M. Toropova[7], E. Unzhakov[12], F. Villante[9,27], A. Vishneva[2], R.B. Vogelaar[16], F.von Feilitzsch[17], H. Wang[22], S. Weinz[23], M. Wojcik [5], M. Wurm[23], Z. Yokley[16], O. Zaimidoroga[2], S. Zavatarelli[3], K. Zuber[21], G. Zuzel [5]

Affiliations for partecipants

[1]AstroParticule et Cosmologie, Univ. Paris Diderot, CNRS/IN2P3, CEA/IRFU, Observatoire de Paris, Sorbonne Paris Cité, 75205 Paris Cedex 13, France

[2]Joint Institute for Nuclear Research, 141980 Dubna, Russia

[3] Dipartimento di Fisica, Università degli Studi e INFN, 16146 Genova, Italy

[4] Institut für Experimentalphysik, Universität Hamburg, 22761 Hamburg, Germany

[5] M. Smoluchowski Institute of Physics, Jagiellonian University, 30348 Krakow, Poland

[6] Kiev Institute for Nuclear Research, 03680 Kiev, Ukraine

[7] National Research Centre Kurchatov Institute, 123182 Moscow, Russia

[8] National Research Nuclear University MEPhI (Moscow Engineering Physics Institute), 115409 Moscow, Russia

[9] INFN Laboratori Nazionali del Gran Sasso, 67010 Assergi (AQ), Italy

[10] Dipartimento di Fisica, Università degli Studi e INFN, 20133 Milano, Italy

[11] Dipartimento di Chimica, Biologia e Biotecnologie, Università degli Studi e INFN, 06123 Perugia, Italy

[12] St. Petersburg Nuclear Physics Institute NRC Kurchatov Institute, 188350 Gatchina, Russia

[13] Physics Department, Princeton University, Princeton, NJ 08544, USA

[14] Chemical Engineering Department, Princeton University, Princeton, NJ 08544, USA

[15] Amherst Center for Fundamental Interactions and Physics Department, University of Massachusetts, Amherst, MA 01003, USA

[16] Physics Department, Virginia Polytechnic Institute and State University, Blacksburg, VA 24061, USA

[17] Physik-Department and Excellence Cluster Universe, Technische Universität München, 85748 Garching, Germany

[18] Lomonosov Moscow State University Skobeltsyn Institute of Nuclear Physics, 119234 Moscow, Russia

[19] Gran Sasso Science Institute, 67100 L'Aquila, Italy

[20] Department of Physics, University of Houston, Houston, TX 77204, USA

[21] Department of Physics, Technische Universität Dresden, 01062 Dresden, Germany

[22] Physics and Astronomy Department, University of California Los Angeles (UCLA), Los Angeles, California 90095, USA

[23] Institute of Physics and Excellence Cluster PRISMA, Johannes Gutenberg-Universität Mainz, 55099 Mainz, Germany

[24] Department of Physics and Astronomy, University of Hawaii, Honolulu, HI 96822, USA

[25] Institut für Kernphysik, Forschungzentrum Jülich, 52425 Jülich, Germany

[26] RWTH Aachen University, 52062 Aachen, Germany

[27] Dipartimento di Scienze Fisiche e Chimiche, Università dell'Aquila, 67100 L'Aquila, Italy

[a]Also at: Laboratorio Subterráneo de Canfranc, Paseo de los Ayerbe S/N, 22880 Canfranc Estacion Huesca, Spain
[b] Present address: Physics Department, University of California, San Diego, CA 92093, USA
[c] Present address: Dipartimento di Fisica, Sapienza Università di Roma e INFN, 00185 Roma, Italy
[d] Present address: Dipartimento di Fisica, Università degli Studi Federico II e INFN, 80126 Napoli, Italy
[e] Present address: Fermi National Accelerator Laboratory (FNAL), Batavia, IL 60510, USA
[f] Present address: Universidad Autónoma de Madrid, Ciudad Universitaria de Cantoblanco, 28049 Madrid, Spain

Background (*LER*)	**rate (Bq/100 t)**
^{14}C(0.156 MeV, β^-)	[40.0 ± 2.0]
Background (*LER*)	**rate (cpd/100 t)**
^{85}Kr (0.687 MeV, β^-) (internal)	6.8 ± 1.8
^{210}Bi (1.16 MeV, β^-) (internal)	17.5 ± 1.9
^{11}C (1.02-1.98 MeV, β^+) (internal)	26.8 ± 0.2
^{210}Po (5.3 MeV, α) (internal)	260.0 ± 3.0
^{40}K (1.460 MeV, γ) (external)	1.0 ± 0.6
^{214}Bi (<1.764 MeV, γ) (external)	1.9 ± 0.3
^{208}Tl (2.614 MeV, γ) (external)	3.3 ± 0.1
Background (*HER-I*)	**rate (cpd/227.8 t)**
μ, cosmogenics, ^{214}Bi (internal)	$[6.1^{+8.7}_{-3.1} 10^{-3}]$
(α , n) (external)	0.224 ± 0.078
^{208}Tl(5.0 MeV, β^-, γ) (internal)	[0.042 ± 0.008]
^{208}Tl(5.0 MeV, β^-, γ) (emanated)	0.469 ± 0.063
^{208}Tl(5.0 MeV, β^-, γ) (surface)	1.090 ± 0.046
Background (*HER-II*)	**rate (cpd/266.0 t)**
μ, cosmogenics (internal)	$[3.8^{+14.6}_{-0.1} 10^{-3}]$
(α , n) (external)	0.239 ± 0.022

Table 1 | ***Rates of residual backgrounds****. List of backgrounds as obtained by the fit to the energy spectrum of collected events in the three energy regions used in this study* (*LER*, *HER-I*, and *HER-II*)*. We report in parenthesis the Q-value and type of particle for each background. The rates in square brackets are estimated independently and are constrained in the fit. Background can be internal (i.e. due to events uniformly distributed in the scintillator volume) or external (i.e. due to events from sources surrounding the scintillator).*

Solar ν	Borexino experimental results Rate (cpd/100 t)	Flux (cm^{-2} s^{-1})	Flux –SSM predictions (cm^{-2} s^{-1})
pp	$134 \pm 10^{+6}_{-10}$	$(6.1 \pm 0.5^{+0.3}_{-0.5}) \times 10^{10}$	$5.98(1. \pm 0.006) \times 10^{10}$ (HZ) $6.03(1. \pm 0.005) \times 10^{10}$ (LZ)
^{7}Be	$48.3 \pm 1.1^{+0.4}_{-0.7}$	$(4.99 \pm 0.11^{+0.06}_{-0.08}) \times 10^9$	$4.93(1. \pm 0.06) \times 10^9$ (HZ) $4.50(1. \pm 0.06) \times 10^9$ (LZ)
pep (HZ)	$2.43 \pm 0.36^{+0.15}_{-0.22}$	$(1.27 \pm 0.19^{+0.08}_{-0.12}) \times 10^8$	$1.44(1. \pm 0.009) \times 10^8$ (HZ) $1.46(1. \pm 0.009) \times 10^8$ (LZ)
pep (LZ)	$2.65 \pm 0.36^{+0.15}_{-0.24}$	$(1.39 \pm 0.19^{+0.08}_{-0.13}) \times 10^8$	$1.44(1. \pm 0.009) \times 10^8$ (HZ) $1.46(1. \pm 0.009) \times 10^8$ (LZ)
$^8B_{HER-I}$	$0.136^{+0.013+0.003}_{-0.013-0.003}$	$(5.77^{+0.56+0.15}_{-0.56-0.15}) \times 10^6$	$5.46(1. \pm 0.12) \times 10^6$ (HZ) $4.50(1. \pm 0.12) \times 10^6$ (LZ)
$^8B_{HER-II}$	$0.087^{+0.080+0.005}_{-0.010-0.005}$	$(5.56^{+0.52+0.33}_{-0.64-0.33}) \times 10^6$	$5.46(1. \pm 0.12) \times 10^6$ (HZ) $4.50(1. \pm 0.12) \times 10^6$ (LZ)
$^8B_{HE}$	$0.223^{+0.015+0.006}_{-0.016-0.006}$	$(5.68^{+0.39+0.03}_{-0.41-0.03}) \times 10^6$	$5.46(1. \pm 0.12) \times 10^6$ (HZ) $4.50(1. \pm 0.12) \times 10^6$ (LZ)
CNO	< 8.1 (95 % C.L.)	$< 7.9 \times 10^8$ (95 % C.L.)	$4.88(1. \pm 0.11) \times 10^8$ (HZ) $3.51(1. \pm 0.10) \times 10^8$ (LZ)
hep	<0.002 (90% C.L.)	$<2.2 \times 10^5$ (90 % C.L.)	$7.98(1. \pm 0.30) \times 10^3$ (HZ) $8.25(1. \pm 0.12) \times 10^3$ (LZ)

Table 2 | **Borexino solar neutrino results.** *Measure rates (first column): for pp, ^{7}Be, pep and CNO neutrinos we quote the total counts without any threshold; for ^{8}B and hep neutrinos we quote the counts above the corresponding analysis threshold. Neutrino fluxes (second column) are obtained from the measured rates assuming the MSW-LMA oscillation parameters[19], standard neutrino-electron cross-sections[27] and a density of electrons in the scintillator of* $(3.307 \pm 0.003) \times 10^{31}$ *e^-/100 tons. All fluxes are integral values without any threshold. The result on pep vs depends on whether we assume high metallicity (HZ) or low metallicity (LZ) Standard Solar Models (SSM) predictions to constrain the CNO ν flux. The last column shows the fluxes predicted by the SSM in the HZ or LZ hypotheses[18].*

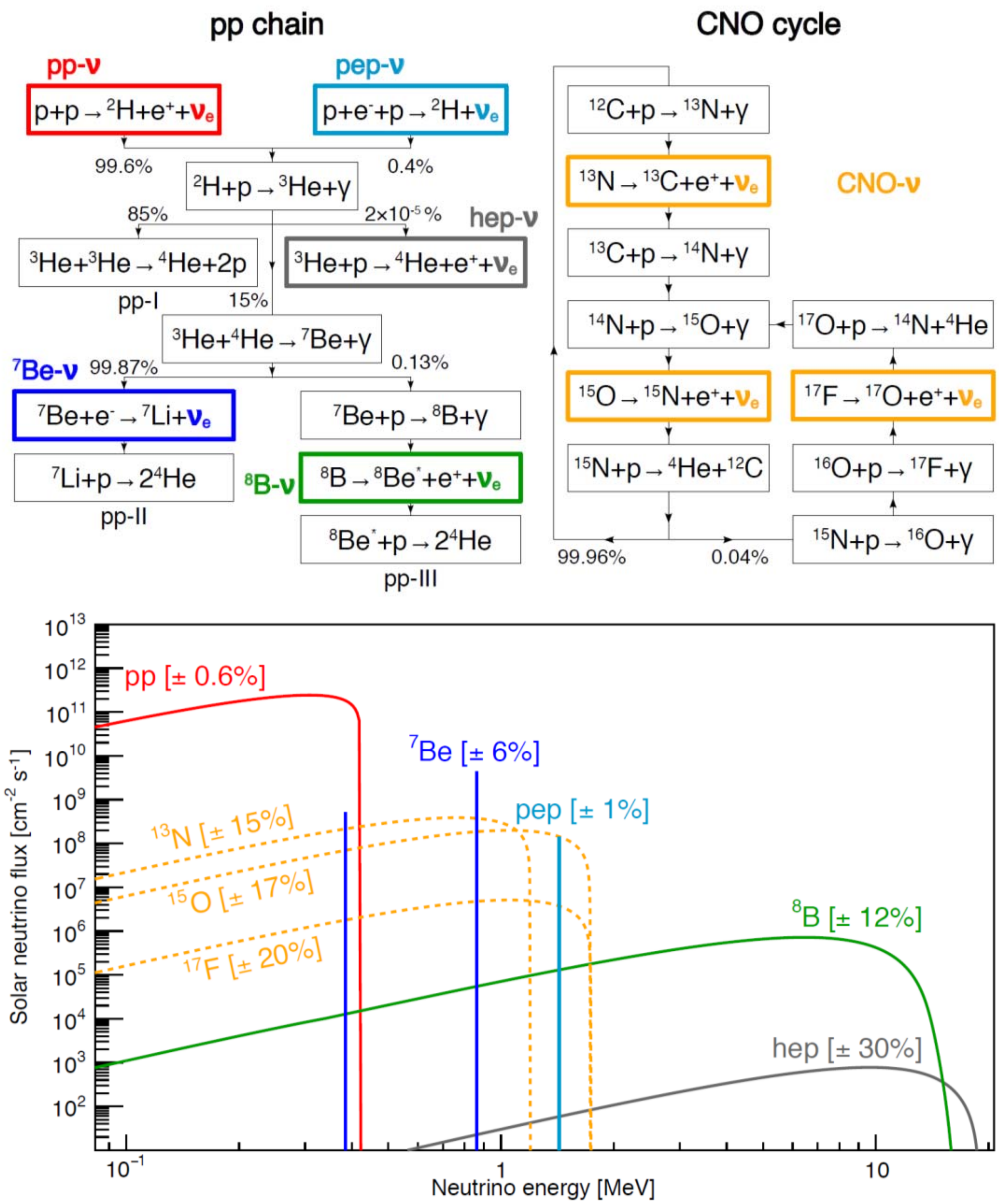

Figure 1| ***Nuclear fusion sequences and neutrino energy spectrum.*** *Schematic view of the pp and CNO nuclear fusion sequences. Solar neutrino energy spectrum from* [18,38]*. The flux (vertical scale) is given in* $cm^{-2}\ s^{-1} MeV^{-1}$ *for continuum sources and in* $cm^{-2}\ s^{-1}$ *for mono-energetic ones.*

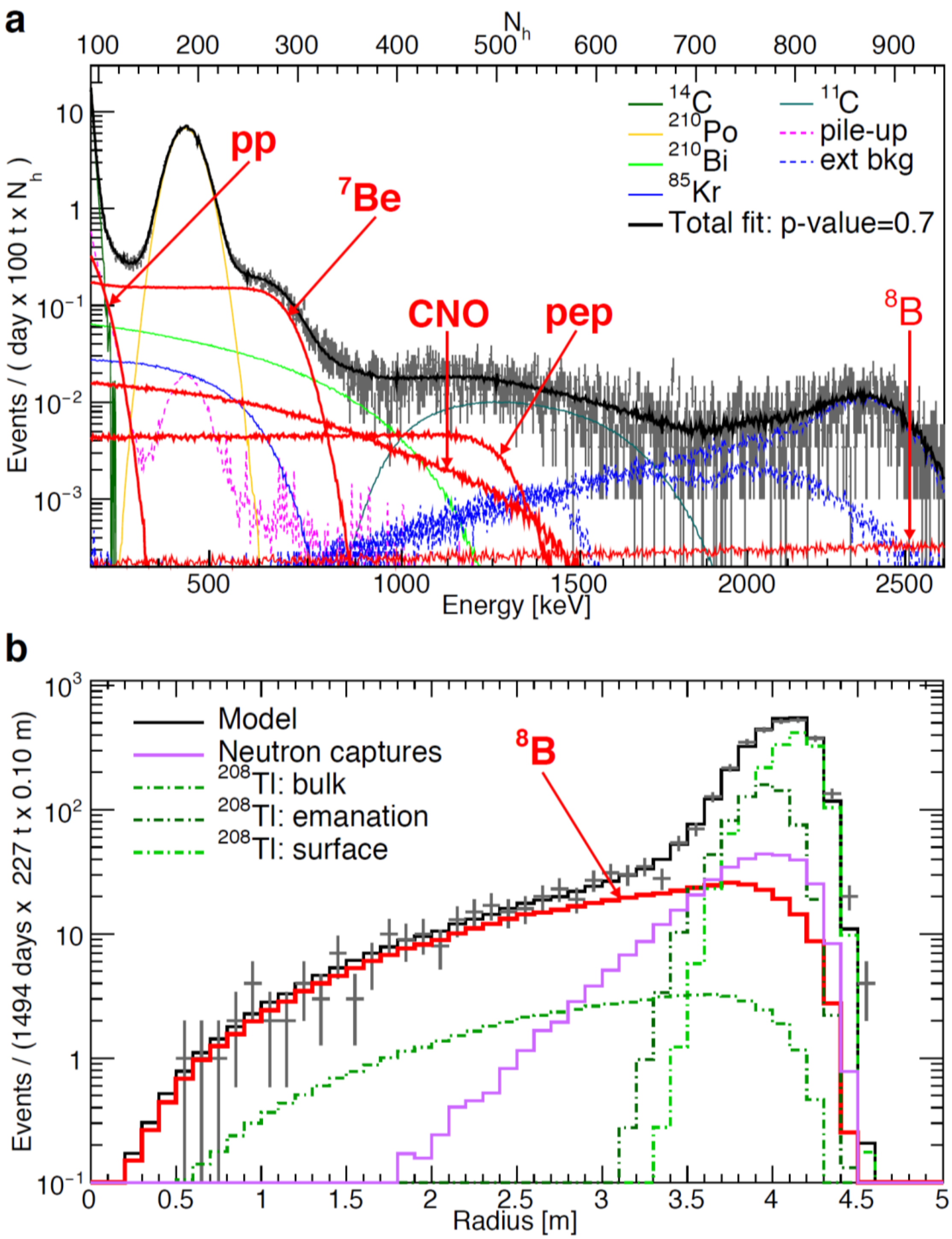

Figure 2| ***Results of the fit to extract the neutrino signal.*** *Distributions of events after selection cuts and corresponding fits with neutrino and background components.* ***a)****: Three Fold Coincidence (TFC)-subtracted energy spectrum with suppressed* ^{11}*C background in LER.* ***b)****: radial distribution of events in HER-I.*

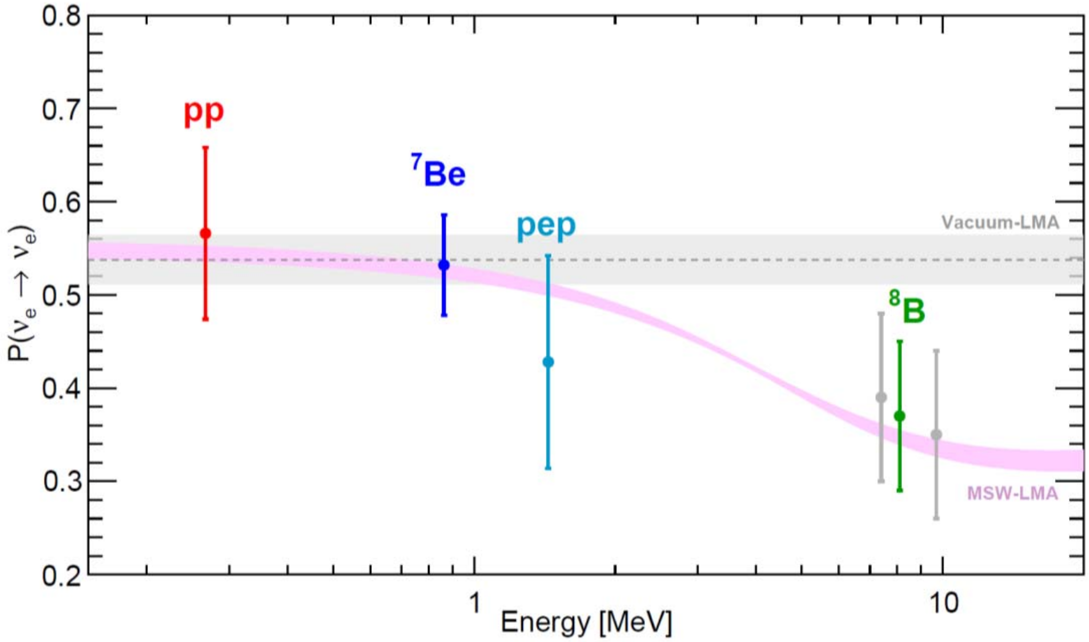

Figure 3| ***Electron neutrino survival probability P_{ee} as a function of neutrino energy.*** *The pink band is the ±1σ prediction of MSW-LMA with oscillation parameters determined from*[19]*. The grey band is the vacuum-LMA case with oscillations parameters determined from*[39,40]*. Data points represent the Borexino results for pp (red), ^{7}Be (blue), pep (cyan), and ^{8}B (green for the HER range, and grey for the separate HER-I and HER-II sub-ranges), assuming high metallicity standard solar model (HZ-SSM). ^{8}B and pp data points are set at the mean energy of neutrinos which produce scattered- electrons above the detection threshold. The error bars include experimental and theoretical uncertainties.*

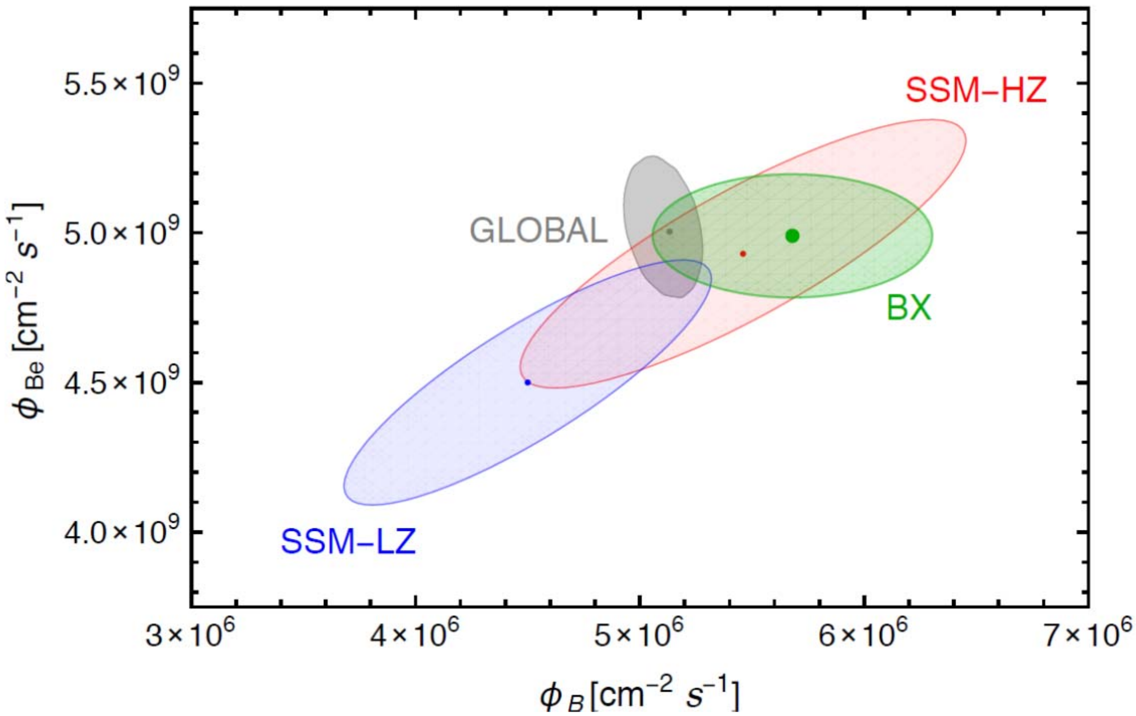

Figure 4|: ***Borexino results and global analysis in the $\Phi(^7Be)$- $\Phi(^8B)$ space.*** *Borexino results for ^7Be and ^8B neutrino fluxes (green point and shaded area). Allowed contours in the $\Phi(^7Be)$- $\Phi(^8B)$ space obtained by combining these new results with all solar and KamLAND data, and leaving free the oscillation parameters θ_{12} and Δm^2_{12}. The theoretical prediction for the low metallicity (LZ)[40](blue) and the high metallicity (HZ)[43] (red) Standard Solar Models (SSM)[18] are also shown. The fit returns the following oscillation parameters: $\tan^2\theta_{12}=0.47\pm0.03$ and $\Delta m^2_{12} = 7.5 \times 10^{-5} \pm0.03$, in agreement with what reported in*[19] *($\sin^2\theta_{13}$ is fixed to 0.0217 [19]). All contours corresponds to 68.27% C.L.*

Methods

The Borexino detector

Borexino is a large liquid scintillator (LS) experiment located deep underground at the Laboratori Nazionali del Gran Sasso in Italy. Borexino is designed to achieve extremely low background conditions. The active core of the detector consists of ~300 t of pseudocumene (1,2,4-trimethylbenzene) doped with 1.5 g/l of PPO (2,5-diphenyloxazole) and contained in a spherical nylon inner vessel (IV, R = 4.25 m). The scintillator is surrounded by a non-scintillating pseudocumene-based buffer liquid which serves as a shield against external radioactivity (see Extended Data Fig. 1). The scintillator fluorescence light is collected by 2212 photomultiplier tubes (PMTs) mounted on a Stainless Steel Sphere with 6.9 m radius. The entire detector is enclosed in a domed, cylindrical tank filled with high-purity water, equipped with 208 PMTs, which provides extra shielding against external radioactivity (photons and neutrons), and also serves as an active water Cherenkov veto against residual cosmic muons.

A detailed description of the Borexino detector is found in[26].

The Standard Solar Model and the solar metallicity controversy

The Standard Solar Model (SSM) is a solution of the stellar evolution equations for stars with $M = M_\odot$ (the solar mass), calibrated to match present-day, measured surface properties of the Sun. A fundamental assumption is that the Sun was initially chemically homogeneous and that along its 4.56 Gyr-long evolution up to the present day, it has modified its chemical composition solely due to nuclear reactions and elemental diffusion. The model calibration is done by adjusting the mixing length parameter and the initial chemical composition in order to reproduce the observed solar luminosity, radius, and current surface composition. As a result of this procedure, the SSM has no free parameters and completely determines the mechanical and thermal properties of the Sun.

The SSM predicts that most of the solar energy (> 99%) is produced by the so-called *pp*-chain (see Fig. 1) that fuses hydrogen into ^{4}He: the chain is initiated by the proton-proton fusion reaction and, to a minor extent, by the alternative three-body proton-electron-proton (*pep*) process. These reactions produce deuterons, which are efficiently converted into ^{3}He by the subsequent deuteron-proton reaction. The *pp*-chain terminates most of the times with the $^3He + ^3He \rightarrow ^4He + 2p$ reaction (*pp*-I termination). In the late '50s, Holmgren and Johnston[39] discovered the cross section for the competing $^3He + ^4He \rightarrow ^7Be + \gamma$ reaction to be about one thousand times larger than previously thought, causing the branching ratios of the *pp*-II and *pp*-III terminations to be not negligible. An alternative process is the so-called CNO cycle, a closed-loop nuclear reaction in which ^{12}C, ^{14}N, and ^{16}O nuclei catalyze hydrogen fusion into ^{4}He. The CNO cycle is a subdominant energy-producing mechanism in stars like the Sun or lighter, but is believed to be the dominant fusion mechanism in heavier or older stars.

For each ^{4}He nucleus produced in the Sun, 2 electron-flavor neutrinos are emitted. Neutrinos free-stream across the solar plasma and reach the Earth traveling close to the speed of light in about 8 minutes, resulting in a total flux of about 6.5×10^{10} cm^{-2} s^{-1}. The solar neutrino spectrum depends on the branching ratios of the different *pp*-chain terminations and on the relative intensity of the *pp*-chain and the CNO-cycle. A large percentage (~90%) of the neutrinos emitted by the Sun are produced in the primary proton-proton fusion reaction (*pp* νs). Most of the remaining 10% of the solar neutrino flux is emitted in the electron capture reaction on ^{7}Be (^{7}Be νs), which appears along the *pp*-II branch of the chain. Smaller contributions come from proton-electron-proton fusion (*pep* νs) and from ^{8}B decays in the *pp*-III branch producing ^{8}B νs. Neutrinos from proton capture on ^{3}He (*hep* νs) are expected to be emitted with negligible probability (10^{-7}) and are beyond current detection sensitivity. The predicted energy spectrum of all neutrinos emitted along the *pp*-chain, including spectral shapes and intensity before neutrino oscillations are shown in Fig. 1.

The predictions of the SSM have been tested by solar neutrino experiments and by helioseismology (which determines the properties of the solar interior by studying the propagation of seismic waves at the Sun's surface). However, important questions about the Sun still call for an answer. The *solar metallicity*, *e.g.*, the abundance of elements heavier than He, is poorly understood, although it is a fundamental input to constructing SSMs and a relevant parameter in astrophysics, since almost all determinations of elemental abundances in astronomical objects rely upon the solar composition. Recent determinations of the solar surface composition[40,41,42] suggest that the solar metallicity might be lower than previously assumed[43,44]. SSMs that incorporate these lower abundances are, however, less in agreement with helioseismic data: this is often referred to as the *solar metallicity* problem.

Solar neutrino measurements provide fundamental clues for the solution of this puzzle. Indeed, the opacity of the solar plasma is strongly influenced by the presence of heavy elements. Since opacity determines the efficiency of radiative energy transfer, the metal content of solar matter affects the temperature profile of the Sun. As a consequence, metallicity determines the branching ratios for the various terminations of the *pp* chain, as well as the relative intensity of the *pp*-chain with respect to the CNO-cycle. A precise determination of the solar neutrino fluxes comprising both the *pp*-chain and CNO-cycle is thus a direct, robust way to settle the solar metallicity controversy. In the main text we compare our experimental results with predictions of high[43] and low[40] metallicity SSMs[18], obtaining a first significant step in this direction.

Neutrino oscillations and the MSW effect

For many years, the experimental results on solar neutrinos have been at odds with the predictions of the Standard Solar Model: all the experiments observed a significant deficit of neutrinos with respect to expectations. This 30-year-long controversy was settled only in 2002 by the experiment SNO[11] which proved unambiguously that the solution to the "solar neutrino problem" was not to be searched in solar physics, but in neutrino physics, namely, in the quantum mechanics phenomenon of flavor oscillations[12]. Through this mechanism, solar neutrinos, which are born in the Sun as ν_e, have a non-zero probability to transform into neutrinos with a different flavor (either ν_μ or ν_τ) during propagation and have therefore reduced probability to be detected on Earth. For oscillations to occur, two conditions must be met: i) mass and flavor eigenstates for neutrinos must not coincide, which implies the existence of a non-trivial mixing matrix which transforms one into the other; ii) the mass of at least one neutrino must be different from 0. The relevant parameters for solar neutrino oscillations are the mixing angle θ_{12} and the squared mass difference between the mass eigenstates mostly contributing to ν_e, *i.e.*, Δm^2_{12}. The probability of flavor conversion is enhanced when neutrinos cross the dense solar medium, because of coherent forward scattering on electrons. This mechanism is referred to as the Wolfenstein-Mikheyey-Smirnov (MSW) matter effect[13,14] and for the specific values of $\Delta^2 m_{12}$ and of the Sun density profile it is fully effective for solar neutrinos with energies greater than ~ 5 MeV. For energies below 1 MeV, the vacuum oscillation mechanism dominates, while a smooth transition occurs in the intermediate energy region. Figure 3 shows the survival probability P_{ee} for ν_e produced in the Sun as a function of the neutrino energy (pink curve) for the oscillation parameters obtained by a global fit to all solar neutrino experiments and KamLAND[19] . The values of $\Delta^2 m_{12}$ (~7.5

$\times 10^{-5}$ eV^2) and of θ_{12} (~33^0) correspond to the so-called Large Mixing Angle solution (LMA) of the solar neutrino problem.

Event selection and residual backgrounds

The analysis starts with data selection aimed at increasing the signal significance over background. The selection criteria, conceptually similar for the low energy (*LER*) and high energy (*HER*) regions, are conceived to: *i)* reject cosmic muons penetrating the mountain shield; *ii)* reduce cosmogenic background, *i.e.* the decays of short-lived radioactive elements produced in muon-induced nuclear spallation processes in the detector; *iii)* select a fiducial volume of the scintillator, optimized separately for the *LER* and *HER-I/II* analysis.

Rejection of muons is achieved by combining the external Cherenkov veto information with a pulse shape analysis of the scintillator signals, and displays an overall efficiency of *99.992%* [30].

The reduction of cosmogenic background is obtained by excluding events collected during a given time Δt following every muon crossing the scintillator.

For the *LER*, a short muon veto time Δt=300 ms is enough to efficiently suppress most relevant cosmogenic isotopes. An exception is ^{11}C (Q = 0.96 MeV, β^+, τ = 29.4 min), which is produced *in situ* by muon spallation, and has a mean lifetime that greatly exceeds the short muon veto time cut. ^{11}C has a fairly constant concentration in the scintillator (~ 30 cpd/100t) determined by the equilibrium between its production and decay rate and cannot be reduced by any purification procedure. It is therefore one of the most significant backgrounds and must be treated with a specific analysis (see next paragraph).

In case of the *HER*, the rejection of cosmogenic background requires a larger time window of Δt =6.5 s to suppress ^{12}B, ^{8}He, ^{9}C, ^{9}Li, ^{8}B, ^{6}He, and ^{8}Li decays. Furthermore, for the *HER* analysis a 2 ms veto is applied after muons that cross the buffer liquid only. This veto aims at rejecting 4.95 MeV γ-rays following the capture of cosmogenic neutrons on ^{12}C nuclei; an additional cut is applied around the capture position of cosmogenic neutrons, when this happens inside the scintillator, to remove ^{10}C (Q = *3.6* MeV, β^+, τ = 27.8s).

Both in the *LER* and in the *HER,* ^{214}Bi and ^{214}Po from the ^{238}U natural decay chain are removed by exploiting the space-time correlation of their fast $\beta + \alpha$ particle delayed coincidence decays.

The analysis in the *LER* and *HER-I/II* use different FVs. The *LER* fiducial volume focuses on suppressing external γ-rays from ^{40}K, ^{214}Bi, and ^{208}Tl contained in materials surrounding the scintillator. It consists of the central 71.3 t of scintillator, selected by applying a radial cut (R<2.8 m) and a cut along the vertical axis ($-1.8<z<2.2$ m). The *HER* is above the energy of the aforementioned γ-rays. The analysis in *HER-I* only requires a z<2.5 m cut to suppress background events related to a small pin hole in the nylon vessel that causes scintillating fluid to leak into the region surrounding it. The total *HER-I* target mass is 227.8 t. The analysis in *HER-II* uses the entire scintillator volume of 266 t. More details on the selection criteria can be found in[24,25,27].

After the selection cuts described above, some residual background remains both in the *LER* and in the *HER*. The *LER* residual background is detailed in Table I, and is mostly due to traces of radioactive isotopes contaminating the scintillator, *i.e.* ^{14}C, ^{210}Po (either from ^{210}Pb decay or out of equilibrium), ^{85}Kr, ^{210}Bi (from ^{210}Pb), and pile-up of uncorrelated events. A small contribution to the *LER* rate also comes from external ^{208}Tl, ^{214}Bi, and ^{40}K γ-rays emerging from materials surrounding the scintillator. In the *LER* fit, ^{14}C rate is quantified and constrained using an independent sample of events acquired without any trigger threshold[25]. The contribution of pile-up, dominated by simultaneous ^{14}C decays at different detector positions, is treated using the following two methods described in [25,29]: in one case, we construct the *pile-up* spectrum starting from real or Monte Carlo data sets; in the other, we convolve all spectral components with a randomly-acquired spectrum (*i.e.* with events acquired with a solicited, external trigger).

The residual backgrounds affecting the *HER–I/II* are also listed in Table I. Part of the internal events (*i.e.*, events uniformly distributed in the scintillator volume) are due to muons, cosmogenic isotopes, and ^{214}Bi decays surviving the cuts. The total contribution of these backgrounds has been evaluated separately for the *HER-I* and the *HER-II*, following the procedure described in[24], and constrained in the fit. In addition, the presence of untagged ^{11}Be (Q = *11.5* MeV, β^-, τ = 19.9 s) is estimated adopting a novel technique based on a multivariate fit, which includes the energy spectrum and the time profile of events with respect to the preceding muon, and is found to be compatible with zero. The *HER-I* is also affected by internal ^{208}Tl decays, which come from the residual ^{232}Th contamination of the LS. In the fit, this rate is constrained to the value obtained by counting the ^{212}Bi-^{212}Po β+α fast delayed coincidences. External ^{208}Tl contamination contributes to the *HER-I* with two distinct components: one from contamination directly on the IV surface, and another from decays of nuclei that have recoiled off the IV into the LS or originated from the volatile progenitor of ^{208}Tl, ^{220}Rn, that has emanated out of the nylon. The rates of both components are left free to vary in the radial fit. Finally, *HER-I* and *HER-II* are also polluted by γ-rays following the capture of radiogenic neutrons produced via (*α, n*) or spontaneous fission reactions of ^{238}U, ^{235}U, and ^{232}Th in the Stainless Steel Sphere and PMTs. This rate too is a free parameter of the fit.

The ^{11}C background

The ^{11}C background is not removed by the short veto cut after muons. To disentangle its contribution from the neutrino signal, we use a *Three-Fold Coincidence* (TFC) method [23,27] that exploits the time and space correlation between muons, the neutrons they produce in combination with ^{11}C, and the subsequent ^{11}C decays. With this method we divide the events passing the selection cuts in two complementary data sets: one is depleted in ^{11}C (TFC-*subtracted*) and preserves (64.28 ± 0.01)% of the total exposure; the other contains (92 ± 4)% of the ^{11}C (TFC-*tagged*). The energy spectra of these two data sets are fitted simultaneously in the multivariate fit (see following paragraph). The residual ^{11}C (e^+) background in the *TFC-subtracted* spectrum is further disentangled from electron-like events by including in the multivariate fit the distribution of a pulse-shape discrimination variable[23,27]. It is in fact observed that the time distribution of scintillation photons slightly differs between e^- and e^+ events, for the following reasons: i) positron produces ortho-positronium 50% of the times which delays the annihilation by ~3 ns[45]; ii) the e^+ energy deposition occurs in multiple sites within the detector, due to the production of annihilation γ-rays. These effects go in the direction of delaying and extending the time distribution of the scintillator pulse for positron with respect to electron events, a handle we exploit for ^{11}C background rejection.

Fitting procedure for extraction of solar neutrino rates

In order to disentangle the neutrino signal rates from the residual background, we apply different fitting strategies for the *LER* and the *HER*. For *LER,* we adopt a multi-variate approach and simultaneously fit the TFC-*subtracted* and the TFC-*tagged* energy spectra, the spatial distribution, and the distribution of the pulse-shape discrimination variable. The spatial distribution is crucial to separate the residual external background component, while the pulse-shape estimator is optimized to separate e^+ from e^-, key to disentangling ^{11}C from the other fit species (see above). The reference radial distributions for external and internal events used in the multi-variate fit are built with a comprehensive Geant4-based Monte Carlo simulation, carefully tuned and validated with calibration data[28,29]. The spectral shapes of signal and background components used in the multivariate fit of the *LER* are also obtained from simulations. In addition, the fit of the energy spectra is performed using analytical spectral functions[25,27], where the non-linearity of the energy scale (due, for example, to ionization quenching and Cherenkov light emission) and the spatially non-uniform detector response are included via *nuisance* parameters, some of which left free to vary in the fit. The reference e^+ pulse-shape distribution used in the *LER* multivariate fit is based on events selected with the TFC method described above, tuned to obtain a nearly pure sample of ^{11}C events. The reference e^- pulse-shape distribution is obtained from simulations and checked on data using electron-like events isolated via the ^{214}Bi -^{214}Po coincidences.

In the *HER-I/II*, the analysis is based on a fit to the radial distribution of the events to separate the ^{8}B ν signal (uniformly distributed in the scintillator) from the external background components. Similarly to the *LER* fit, the reference radial distributions for external and internal events used in the *HER* fit are built with Geant4-based Monte Carlo simulations.

For more details on the fit to extract the neutrino signal see [27].

Systematic uncertainties in the analysis

The detector energy response and uniformity has been carefully studied by means of an extensive calibration campaign which was carried out in 2009 [28]. The calibration data were used to tune the input parameters of the Borexino Monte Carlo package, a custom Geant4-based code which can simulate all processes following the interaction of a particle in the detector, including all known characteristics of the apparatus[29]. After tuning, the agreement between Monte Carlo and calibration data is very good for both the *LER* and the *HER*: for the energies relevant to the *LER* analysis, the overall uncertainty is below 1%, while for the *HER* analysis, it is around 1.9%.

In spite of this remarkable understanding of the detector response throughout the scintillator volume and in a large energy range, an extensive study of possible sources of systematic errors has been performed both for the *LER* and for the *HER*. The results of these studies are summarized in Extended Data Table 1 and 2, respectively.

Concerning the analysis in the *LER*, the main contribution to the systematic error comes from the fit model, i.e., possible residual inaccuracies in the modelling of the detector response (energy scale, uniformity of the energy response, pulse-shape discrimination shape) and uncertainties in the theoretical energy spectra used in the fit. These systematic effects have been estimated by means of a toy-MC method: an ensemble of 100000 data-sets are simulated from a family of PDF’s which includes deformations due to the inaccuracies under study. The magnitude of the deformations was chosen to be within the range allowed by the available calibration data. These data are then fitted following the same procedure used for real data and differences in the results are quoted as systematics (first line in Extended Data Table 1).

The second source of systematics is related to the fit method, *i.e.*, whether the reference PDF’s used in the fit are entirely derived from Monte Carlo simulations or analytically. Further systematic effects arise from the choice of the energy estimator, from the details of the implementation of the pile-up of uncorrelated events, from using different fit energy ranges and binning, from the inclusion of an independent constraint on ^{85}Kr obtained from its sub-dominant (BR=0.43%) delayed coincidence decay, and from the estimation of the target fiducial mass. This last uncertainty is determined with calibration data, by using sources deployed in known positons throughout the detector volume.

Concerning the *HER* analysis, the most important systematic uncertainties arise from the determination of the target mass, from the energy scale, and from the *z*-cut applied in the *HER-I* range (see Extended Data Table 2).

The target mass uncertainty is related to the fact that the amount of scintillator contained in the Inner Vessel is slowly decreasing (by less than 0.5 m^3/year), due to a small pin-hole in the nylon membrane. We monitor the evolution of the scintillator mass on a week-by-week basis, by studying the Inner Vessel shape which is obtained from the spatial distribution of its surface contamination. This method gives an average total mass of 266 tons with an error of about 2%.

The impact of the uncertainty of the energy scale on the number of events falling in the *HER-I* and *HER-II* energy window has been evaluated with a full Monte Carlo simulation and has been included in the systematic error (second line of Extended Data Table 2).

As mentioned in the main text, the *HER-I* analysis requires a cut on the vertical coordinate to remove background events due to a small pin-hole in the nylon vessel which causes the scintillator to leak into the buffer liquid. In order to estimate possible systematics associated to this cut, the *HER-I* analysis has been performed with a modified z-cut, ± 0.5 m around the chosen value (2.5 m). Differences in the results have been included as systematic error.

Frequentist hypothesis test of MSW vs vacuum oscillations

Borexino provides results on the electron neutrino survival probability (P_{ee}) in the entire solar neutrino energy range.

We are therefore able of performing a statistical study to compare the compatibility of our measurement with two different hypotheses: the standard oscillation scenario, MSW-LMA, and the vacuum-LMA, where matter effect are not present (which is taken as our null-hypothesis).

The survival probability $P_{ee}^{MSW-LMA}$ in the MSW-LMA scenario depends not only on the oscillation parameters θ_{12}, θ_{13}, Δm^2_{12} valid in vacuum, but also on the neutrino-energy E_ν dependent potential characterizing interaction of neutrinos with the dense solar core. It can be expressed as follows[48] :

$$P_{ee}^{MSW-LMA} = \frac{1}{2}\cos^4\theta_{13}(1+\cos 2\theta_{12}^{M}\cos 2\theta_{12})$$

$$\cos 2\theta_{12}^{M} = \frac{\cos 2\theta_{12}-\beta}{\sqrt{(\cos 2\theta_{12}-\beta)^2+\sin^2 2\theta_{12}}}$$

$$\beta = \frac{2\sqrt{2}G_F cos^2\theta_{13} n_e E_\nu}{\Delta m_{12}},$$

where G_F is the Fermi coupling constant and n_e is the density of electrons in the matter. Using the current set of oscillation parameters and errors derived in[19], and following the same procedure described in [27], we obtain the pink band in Fig. 3.

If matter effects were not present, the survival probability for solar neutrinos would be approximated by the espression P_{ee}^{Vac}:

$$P_{ee}^{Vac} = \cos^4\theta_{13}(1 - \frac{1}{2}\sin^2 2\theta_{12}) + \sin^4\theta_{13},$$

which is independent from the neutrino energy E_ν. Taking for θ_{13} and θ_{12} the values and errors measured by reactor neutrino experiments in[39,40], the survival probability P_{ee}^{Vac} as a function of E_ν corresponds to the grey band in Fig. 3.

We performed a frequentist analysis, in which we adopt a test statistics t based on the ratio between the likelihood obtained assuming MSW-LMA and vacuum-LMA:

$t = -2\log[\mathcal{L}(\text{MSW})/\ \mathcal{L}(\text{vacuum})] = \chi^2\ (\text{MSW}) - \chi^2\ (\text{vacuum})$

The probability distribution of t is built with a toy-MC method: we randomly generate thousands of values of P_{ee} in the MSW-LMA hypothesis (by sampling the pink curve in Fig. 3 and including both theoretical and experimental uncertainties) and for each set of data we estimate t and build its distribution (red curve on the left in Extended Data Fig. 2). In the same way, we simulate thousands of P_{ee} values in the vacuum-LMA hypothesis and we build the corresponding t distribution (blue curve on the right in Extended Data Fig. 2).

The actual Borexino results on P_{ee} for *pp,* ^{7}Be, *pep,* and ^{8}B gives a value of t_{BX} = -4.16 (indicated as a dashed line in Extended Data Fig. 2), which allows us to disfavor the vacuum-LMA hypothesis with a p-value of 0.018 (integral of the small tail of the blue curve to the left of t_{BX}), corresponding to a confidence level C.L. of 98.2%.
For more details on the choice of the test statistics see [49].

Frequentist and Bayesian hypothesis test of the HZ vs LZ models

The combination of the Borexino measurement on ^{8}B and ^{7}Be fluxes provides an interesting hint in favour of the solar temperature profile predicted by the HZ metallicity SSM. This was obtained performing both a frequentist and a Bayesian hypothesis test.
In the frequentist analysis, we have used a test statistics t based on the ratio between the likelihood obtained assuming HZ and LZ:
$t = -2\log[\mathcal{L}(HZ)/\mathcal{L}(LZ)] = \chi^2(HZ) - \chi^2(LZ)$.
The probability distribution of t is built with a toy-MC method (full Neumann construction of the confidence intervals): we randomly generate thousands of fake ^{7}Be-^{8}B results in the HZ hypothesis (sampling a distribution which includes both theoretical and experimental errors) and for each set of data we estimate t (red distribution on the left in Extended Data Fig. 3). In the same way, we simulate thousands of fake ^{7}Be-^{8}B results in the LZ hypothesis and we build the corresponding t distribution (in blue on the right in Extended Data Fig. 3).
The value of t corresponding to the actual Borexino result on ^{7}Be -^{8}B is shown in the plot as the dotted line at t_{BX} =-3.49, relatively far from the maximum of the LZ probability distribution (blue curve). This allows us to disfavor the LZ hypothesis with a p-value of 0.034 (integral of the small tail of the blue curve to the left of t_{BX}), corresponding to a confidence level C.L. of 96.6%.
The result is slightly better than the median p-value expected (0.058) which corresponds to a median significance of 94.2% C.L.
For more details on the choice of the test statistics see [49].

In the Bayesian analysis we have constructed two models, one for the HZ and the other for the LZ hypothesis, in which the free parameters are the fluxes of ^{8}B and of ^{7}Be. The model predictions are used as prior probability distributions. The likelihood is constructed as the sum of two Gaussian measurements, one for the flux of ^{8}B and the other for the flux of ^{7}Be.
We perform the comparison of the two models assuming that they have the same probability a priori (50% for the HZ hypothesis and 50% for LZ hypothesis). Coherently to the frequentist analysis, the data show a mild preference for HZ with respect to LZ. The odds are 5:1 or, equivalently, the Bayes factor is 4.9.
For more details on the Bayesian method see [37].

Data availability statement

The datasets generated during the current study are freely available in the repository https://bxopen.lngs.infn.it/. Additional information are available from the spokesperson (spokesperson-borex@lngs.infn.it upon reasonable request.

Reference in Methods

41. Holmgren, H. & Johnston, R., $He^3(\alpha,\gamma)Li^7$ and $He^3(\alpha,\gamma)Be^7$ Reactions. *Phys. Rev.* **113**, 1556 (1959).

42. Asplund, M., Grevesse, N., Sauval, A. J. and Scott, P., The chemical composition of the Sun. *Ann. Rev. Astron. Astrophys.* **47,** 481 (2009).

43. Caffau, E., Ludwig, H. G., Steffen, M., Freytag, B., Bonifacio, P., Solar Chemical Abundances Determined with a CO5BOLD 3D Model Atmosphere. *Solar Physics* **268**, 255 (2011).

44. Asplund, M., Grevesse, N., Sauval, A. J., The Solar chemical composition. *Astronomical Society of the Pacific Conference Series* **336**, 25 (2005), T.G. Barnes and F.N. Bash editors.

45. Grevesse, N., Sauval, A. J., Standard solar compositon. *Space Sci.Rev.* **85**, 161 (1998).

46. Grevesse, N., Noels, A., Cosmic abundances of the elements. *Origin and Evolution of the Elements,* 15 (1993), N. Prantzos, E. Vangioni-Flam, M. Casse editors.

47. Franco, D., Consolati, G. and Trezzi, D., Positronium signature in organic liquid scintillators for neutrino experiments. *Phys. Rev.* C **83**, 015504 (2011).

48. Bahcall, J. N. And Pena-Garay, C, Solar models and solar neutrino oscillations. *New Journal of Phys.* **6**, 63 (2004).

49. Blennow, M., Coloma, P., Quantifying the sensitivity of oscillation experiments to the neutrino mass ordering. JHEP **03**, 028 (2013).

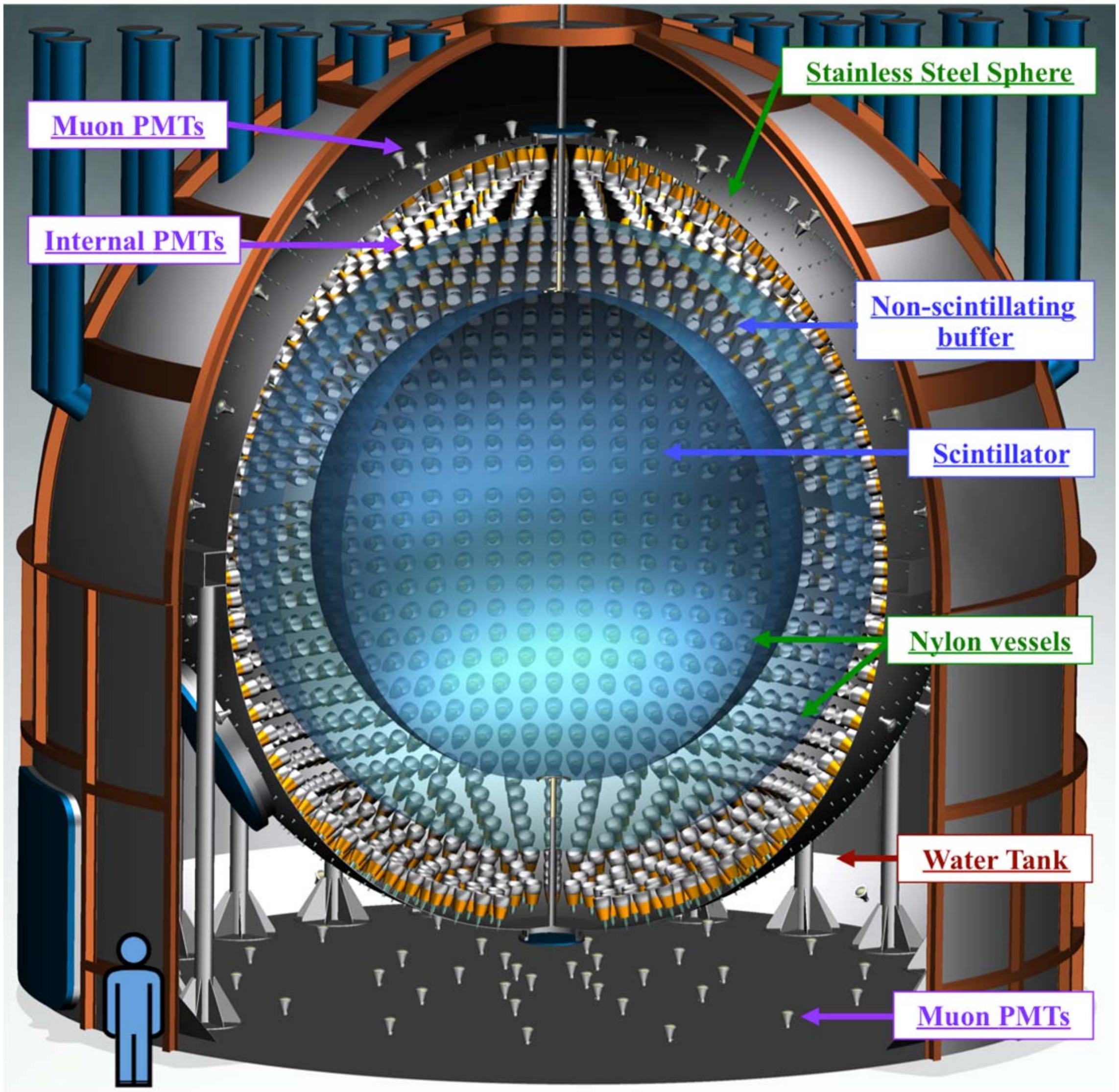

Extended Data Figure 1|: **The Borexino detector.** *Schematic view of the ``onion-like'' structure of the Borexino apparatus. From outside to inside: the external water tank; the Stainless Steel Sphere where ~ 2200 photomultiplier tubes are mounted; the outermost nylon vessel which serves as a barrier against radon; the innermost nylon vessel which contains 300 t of liquid scintillator, the active detection medium.*

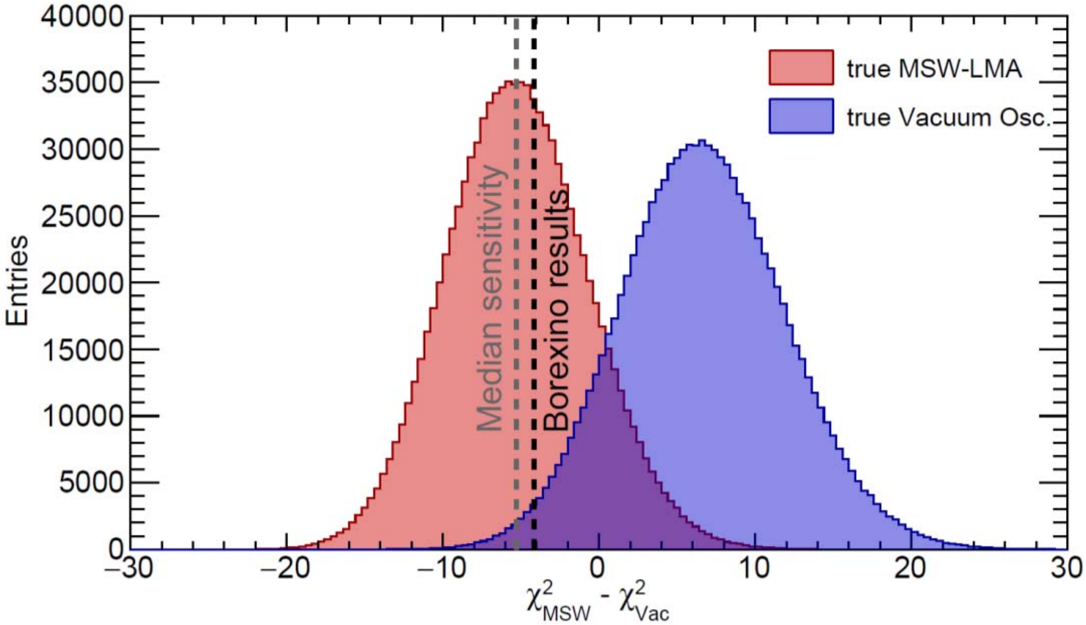

Extended Data Figure 2|: ***Frequentist hypothesis test of MSW-LMA vs vacuum-LMA.*** *The probability distribution of the test statistics t is obtained by simulating thousands of sets of P_{ee} values (at the pp, ^{7}Be, pep, and ^{8}B energies) in the MSW-LMA (*Mikheyev Smirnov Wolfenstein-Large Mixing Angle) *hypothesis (red curve on the left) and in the vacuum-LMA (vacuum-Large Mixing Angle) hypothesis (blue curve on the right). The dotted black line corresponds to the results of Borexino discussed in the main text.*

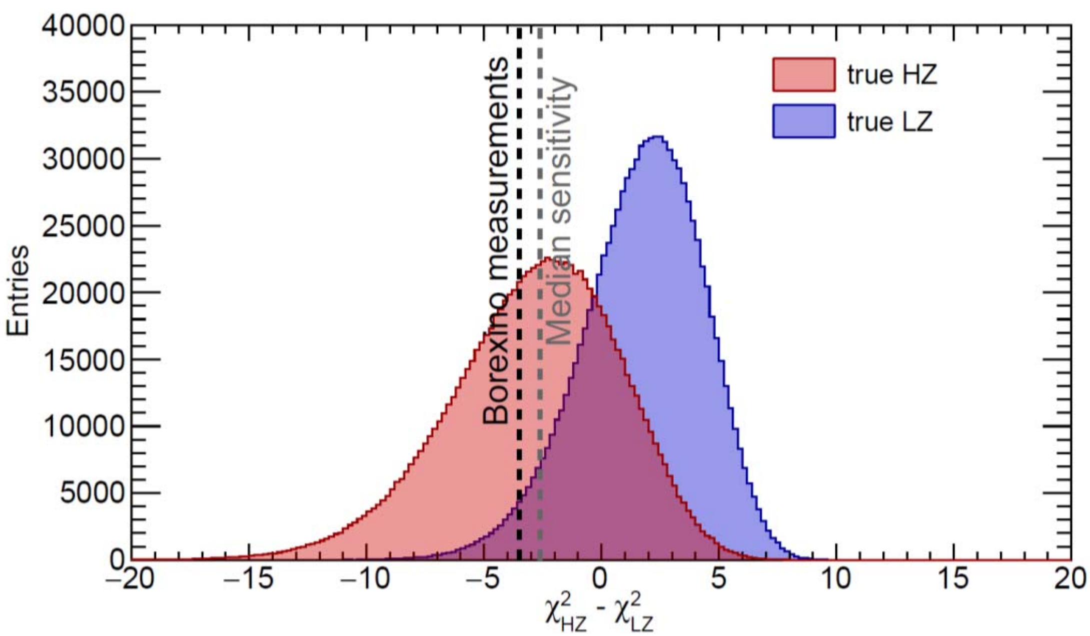

Extended Data Figure 3|: ***Frequentist hypothesis test for LZ and HZ.*** *The probability distribution of the test statistics t is obtained by simulating thousands of fake sets of ^{8}B-^{7}Be values in the high metallicity (HZ) hypothesis (red curve on the left) and in the low metallicity*

(LZ) hypothesis (blue curve on the right). The dotted black line corresponds to the results of Borexino discussed in the main text.

Systematic errors in the *LER* analysis						
	***pp* neutrinos**		**7Be neutrinos**		***pep* neutrinos**	
Source of uncertainty	**-%**	**+%**	**-%**	**+%**	**-%**	**+%**
Fit models (see text)	-4.5	+0.5	-1.0	+0.2	-6.8	+2.8
Fit method (analytical/MC)	-1.2	+1.2	-0.2	+0.2	-4.0	+4.0
Choice of the energy estimator	-2.5	+2.5	-0.1	+0.1	-2.4	+2.4
Pile-up modeling	-2.5	+0.5	0	0	0	0
Fit range and binning	-3.0	+3.0	-0.1	+0.1	-1.0	+1.0
Inclusion of the 85Kr constraint	-2.2	+2.2	0	+0.4	-3.2	0
Live Time	-0.05	+0.05	-0.05	+0.05	-0.05	+0.05
Scintillator Density	-0.05	+0.05	-0.05	+0.05	-0.05	+0.05
Fiducial Volume	-1.1	+0.6	-1.1	+0.6	-1.1	+0.6
Total systematics (%)	**-7.1**	**+4.7**	**-1.5**	**+0.8**	**-9.0**	**+5.6**

Extended data Table 1|: ***LER analysis systematics****. Relevant sources of systematic uncertainties and their contribution to the measured neutrino interaction rates for the LER analysis.*

Systematic errors in the *HER* analysis (8B neutrinos)						
	HER-I		***HER-II***		***HER* (tot)**	
Source of uncertainty	**-%**	**+%**	**-%**	**+%**	**-%**	**+%**
Target Mass	-2.0	+2.0	-2.0	+2.0	-2.0	+2.0
Energy scale	-0.5	+0.5	-4.9	+4.9	-1.7	+1.7
z-cut	-0.7	+0.7	0	0	-0.4	+0.4
Live time	-0.05	+0.05	-0.05	+0.05	-0.05	+0.05
Scintillator density	-0.05	+0.05	-0.05	+0.05	-0.05	+0.05
Total systematics (%)	**-2.2**	**+2.2**	**-5.3**	**+5.3**	**-2.7**	**+2.7**

Extended data Table 2|: ***HER analysis systematics****. Relevant sources of systematic uncertainties and their contribution to the measured neutrino interaction rates for the HER analysis.*

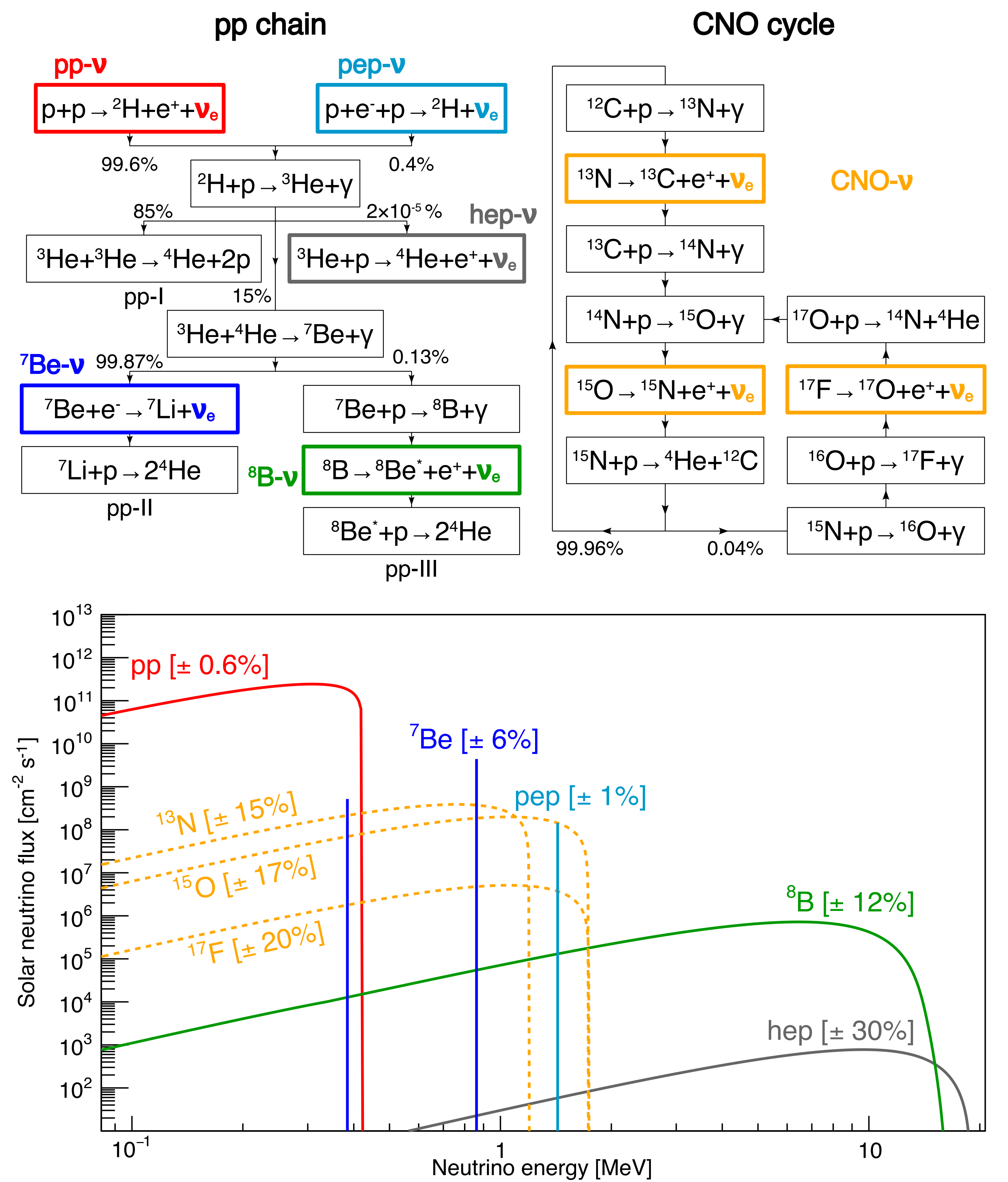

pp chain
CNO cycle
pp-ν
$p+p \rightarrow {}^{2}H+e^{+}+\nu_e$
pep-ν
$p+e^{-}+p \rightarrow {}^{2}H+\nu_e$
99.6%
0.4%
$^{2}H+p \rightarrow {}^{3}He+\gamma$
85%
2×10^{-5} %
hep-ν
$^{3}He+{}^{3}He \rightarrow {}^{4}He+2p$
$^{3}He+p \rightarrow {}^{4}He+e^{+}+\nu_e$
pp-I
15%
$^{3}He+{}^{4}He \rightarrow {}^{7}Be+\gamma$
^{7}Be-ν
99.87%
0.13%
$^{7}Be+e^{-} \rightarrow {}^{7}Li+\nu_e$
$^{7}Be+p \rightarrow {}^{8}B+\gamma$
$^{7}Li+p \rightarrow 2{}^{4}He$
^{8}B-ν
$^{8}B \rightarrow {}^{8}Be^{*}+e^{+}+\nu_e$
pp-II
$^{8}Be^{*}+p \rightarrow 2{}^{4}He$
pp-III
$^{12}C+p \rightarrow {}^{13}N+\gamma$
$^{13}N \rightarrow {}^{13}C+e^{+}+\nu_e$
CNO-ν
$^{13}C+p \rightarrow {}^{14}N+\gamma$
$^{14}N+p \rightarrow {}^{15}O+\gamma$
$^{17}O+p \rightarrow {}^{14}N+{}^{4}He$
$^{15}O \rightarrow {}^{15}N+e^{+}+\nu_e$
$^{17}F \rightarrow {}^{17}O+e^{+}+\nu_e$
$^{15}N+p \rightarrow {}^{4}He+{}^{12}C$
$^{16}O+p \rightarrow {}^{17}F+\gamma$
$^{15}N+p \rightarrow {}^{16}O+\gamma$
99.96%
0.04%
pp [± 0.6%]
^{7}Be [± 6%]
pep [± 1%]
^{13}N [± 15%]
^{15}O [± 17%]
^{17}F [± 20%]
^{8}B [± 12%]
hep [± 30%]
Solar neutrino flux [cm^{-2} s^{-1}]
10^{13}
10^{12}
10^{11}
10^{10}
10^{9}
10^{8}
10^{7}
10^{6}
10^{5}
10^{4}
10^{3}
10^{2}
10^{-1}
1
10
Neutrino energy [MeV]

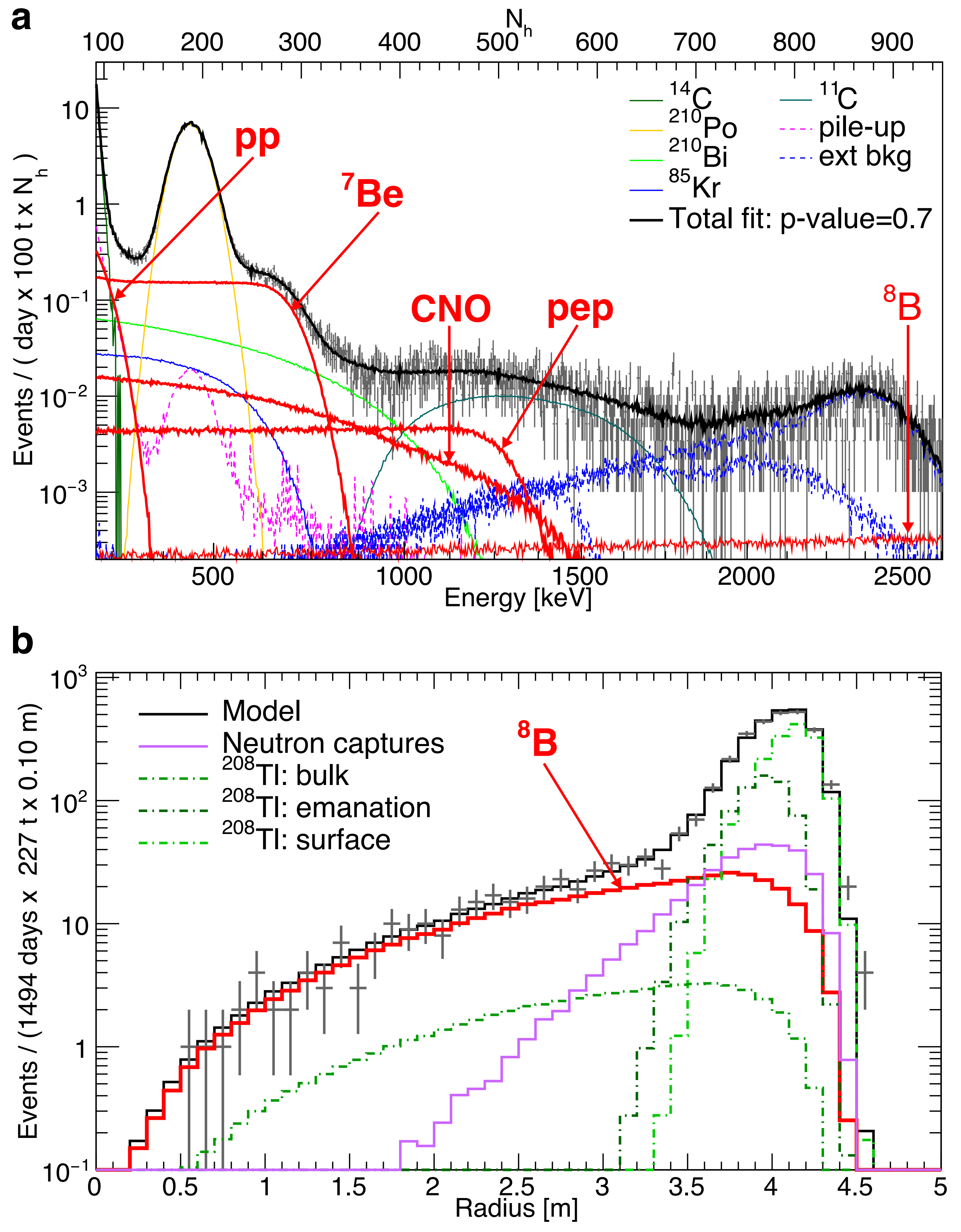

a
N_h
100
200
300
400
500
600
700
800
900
Events / (day x 100 t x N_h)
10
1
10^-1
10^-2
10^-3
14C
210Po
210Bi
85Kr
11C
pile-up
ext bkg
Total fit: p-value=0.7
pp
7Be
CNO
pep
8B
500
1000
1500
2000
2500
Energy [keV]
b
Events / (1494 days x 227 t x 0.10 m)
10^3
10^2
10
1
10^-1
Model
Neutron captures
208Tl: bulk
208Tl: emanation
208Tl: surface
8B
0
0.5
1
1.5
2
2.5
3
3.5
4
4.5
5
Radius [m]

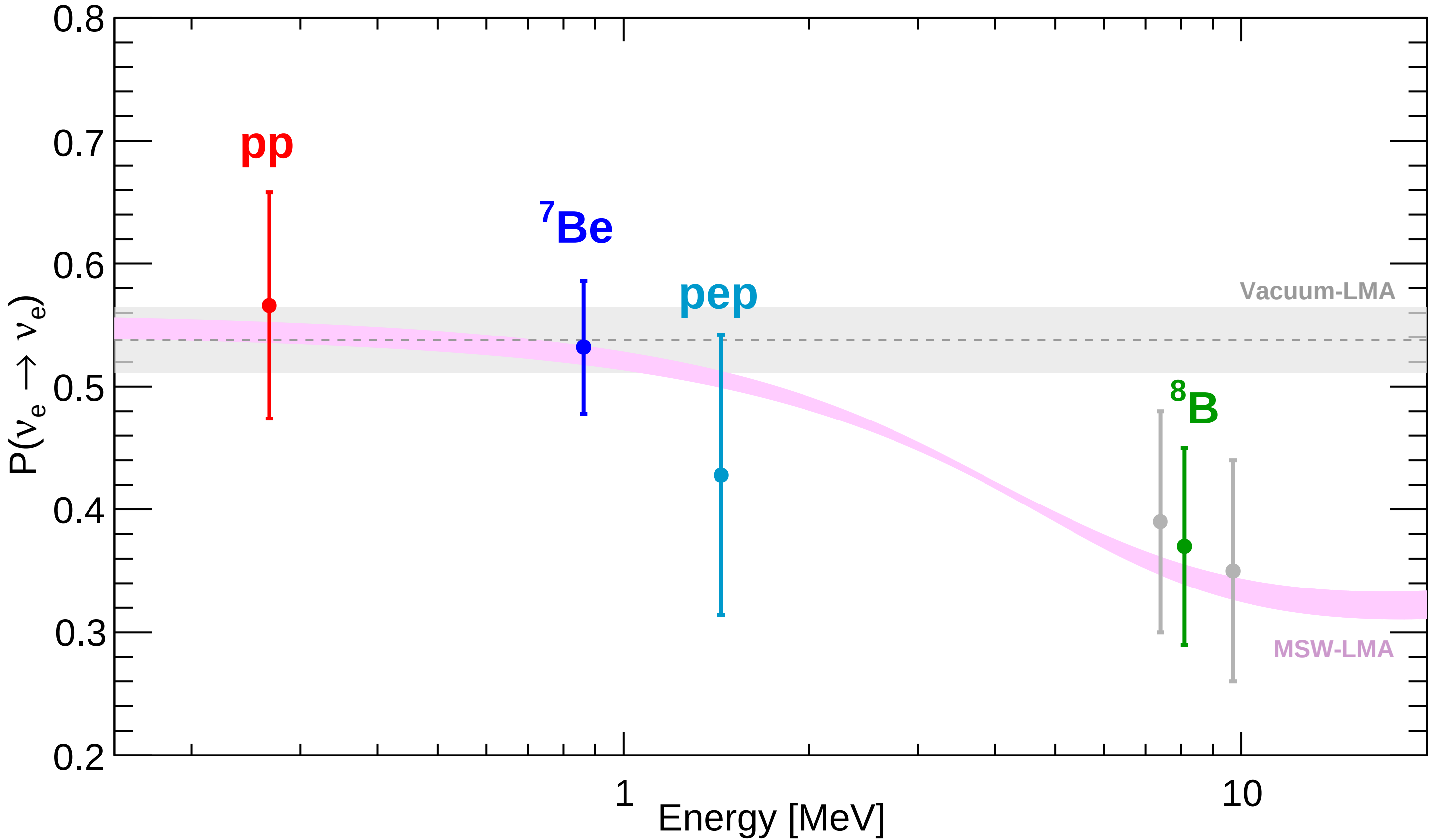

0.8
0.7
0.6
0.5
0.4
0.3
0.2
$P(\nu_e \rightarrow \nu_e)$
pp
^{7}Be
pep
^{8}B
Vacuum-LMA
MSW-LMA
1
10
Energy [MeV]

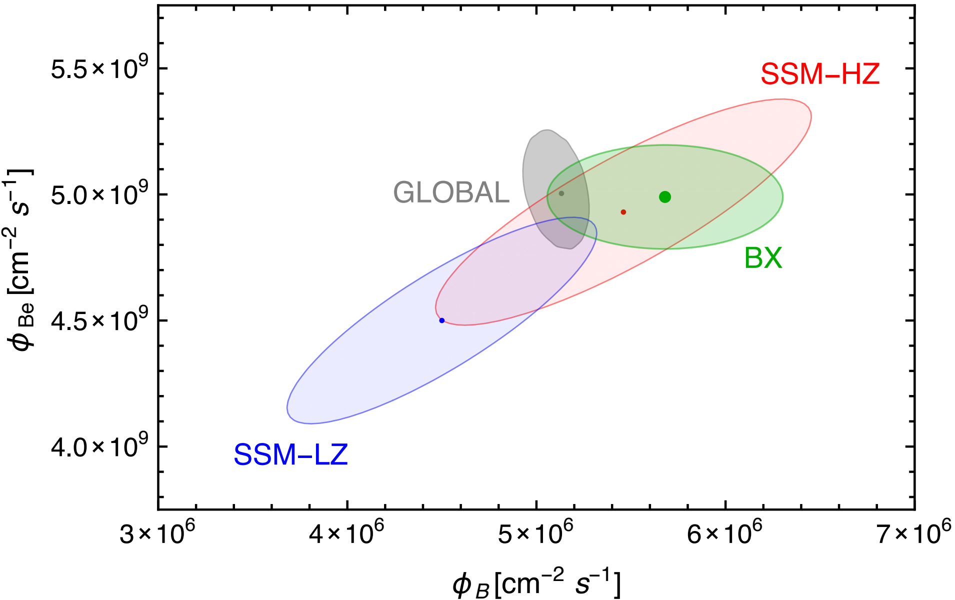

SSM−HZ
GLOBAL
BX
SSM−LZ
5.5×10^9
5.0×10^9
4.5×10^9
4.0×10^9
3×10^6
4×10^6
5×10^6
6×10^6
7×10^6
ϕ_{Be} [cm^{-2} s^{-1}]
ϕ_B [cm^{-2} s^{-1}]